

# Time delay measurements with Broken Power Law model

Guanhua Rui,<sup>1,2</sup> Bin Hu,<sup>1,2</sup> Wei Du<sup>3</sup>†

<sup>1</sup>*Institute for Frontier in Astronomy and Astrophysics, Beijing Normal University, Beijing, 102206, China*

<sup>2</sup>*School of Physics and Astronomy, Beijing Normal University, Beijing 100875, China*

<sup>3</sup>*Shanghai Key Lab for Astrophysics, Shanghai Normal University, Shanghai, 200234, China*

Accepted XXX. Received YYY; in original form ZZZ

arXiv:2601.09369v1 [astro-ph.CO] 14 Jan 2026

## ABSTRACT

One of the key challenges in strong gravitational lensing cosmography is the accurate measurement of time delays between multiple lensed images, which are essential for constraining the Hubble constant ( $H_0$ ). In this study, we investigate how assumptions about the lens mass profile affect time-delay measurements in strong lensing systems. Specifically, we implement a Broken Power Law (BPL) mass model within the LENSTRONOMY framework (Birrer & Amara 2018), which introduces additional flexibility in the radial mass distribution and can phenomenologically capture deviations from a single power-law profile. This model is combined with a numerical approach to compute time delays at the image positions. We validate the BPL implementation using simulated lens systems and compare the results with those obtained from the commonly adopted elliptical power-law (EPL) model. We then apply both model families to the quadruply imaged quasar WGD 2038–4008. Both models fit the imaging and kinematic data comparably well, yet the greater radial freedom in the BPL model shifts the inferred time-delay distance—and thus  $H_0$ —by an amount comparable to the current discrepancy between early- and late-universe estimates of the Hubble constant. In a flat  $\Lambda$ CDM cosmology, the Hubble constant inferred using the BPL lens model is  $H_0 = 75^{+23.1}_{-16.3} \text{ km s}^{-1} \text{ Mpc}^{-1}$ , while the EPL model gives  $H_0 = 61^{+19.2}_{-13.2} \text{ km s}^{-1} \text{ Mpc}^{-1}$ . This difference is largely due to uncertainties in the inner mass profile ( $\theta < 0''.2$ ), a region where point spread function (PSF) reconstruction is a critical factor—a finding consistent with results reported in Shajib et al. (2022). This highlights how time-delay cosmography remains sensitive to assumptions about the lens mass profile. With current precision, this difference does not favor one cosmological scenario over another, but rather underscores the importance of flexible mass modeling and PSF modeling.

**Key words:** cosmology: distance scale – gravitational lensing: strong – dark matter

## 1 INTRODUCTION

The Hubble constant ( $H_0$ ) characterizes the present-day expansion rate of the Universe, yet its precise value remains one of the most significant unresolved issues in modern cosmology. The so-called Hubble tension refers to the discrepancy, now exceeding the  $5\sigma$  level, between early-universe determinations based on the cosmic microwave background (CMB) and late-universe measurements relying on the distance ladder (Verde et al. 2019). Within the standard  $\Lambda$ CDM framework, CMB observations from the *Planck* satellite imply  $H_0 \simeq 67 \text{ km s}^{-1} \text{ Mpc}^{-1}$ , in agreement with other early-universe probes (Collaboration et al. 2020). In contrast, direct local measurements yield systematically higher values: the SH0ES collaboration reports  $H_0 = 73.04 \pm 1.04 \text{ km s}^{-1} \text{ Mpc}^{-1}$  from Cepheid-calibrated Type Ia supernovae (Riess et al. 2022), with independent methods such as megamaser distances providing consistent results (e.g.  $H_0 = 73.9 \pm 3.0 \text{ km s}^{-1} \text{ Mpc}^{-1}$ ; Pesce et al. 2020). Alternative distance-ladder calibrations based on the tip of the red giant branch yield intermediate values around  $H_0 \simeq 69\text{--}70 \text{ km s}^{-1} \text{ Mpc}^{-1}$  (Freedman 2021). Meanwhile, inverse distance-ladder and large-scale structure analyses, including baryon acoustic oscillations and galaxy sur-

veys, generally recover  $H_0 \simeq 67\text{--}68 \text{ km s}^{-1} \text{ Mpc}^{-1}$ , consistent with the CMB results (e.g., Abbott et al. 2018; Addison et al. 2018). The persistence of this tension across multiple, largely independent observational approaches has motivated renewed scrutiny of potential systematic uncertainties and the exploration of extensions beyond the standard  $\Lambda$ CDM model (Verde et al. 2019).

Strong gravitational lensing time-delay cosmography provides an independent, one-step geometric method for measuring the Hubble constant  $H_0$ . This technique exploits the relative arrival times between multiple images of a variable background source, such as quasar or supernova, produced by the gravitational potential of a foreground galaxy. By jointly modeling the lens mass distribution and incorporating the source and deflector redshifts, one can infer the time-delay distance  $D_{\Delta t}$ , which scales inversely with  $H_0$  for a given cosmological model (Suyu et al. 2010; Treu & Marshall 2016). As a result, time-delay cosmography does not rely on either local distance ladders or early-universe physics, making it a valuable and complementary probe for addressing the Hubble tension. Using six quadruply imaged quasars with high-quality HST imaging, time-delay measurements, stellar kinematics, and detailed characterization of the lens environment, the H0LiCOW collaboration reported  $H_0 = 73.3^{+1.7}_{-1.8} \text{ km s}^{-1} \text{ Mpc}^{-1}$  in a flat  $\Lambda$ CDM cosmology (Wong et al. 2020). A subsequent joint analysis of seven lenses by H0LiCOW and STRIDES yielded a consistent result of  $H_0 = 73.9^{+1.8}_{-1.8} \text{ km s}^{-1} \text{ Mpc}^{-1}$

\* E-mail: bhu@bnu.edu.cn

† E-mail: duwei@shnu.edu.cn

under similar modeling assumptions (Shajib et al. 2020). Alternative strong-lensing approaches, including free-form mass modeling, have obtained compatible values of  $H_0$ , supporting the robustness of time-delay measurements when imaging and time-delay information dominate the inference (Jee et al. 2019). More recent analyses by the TDCOSMO collaboration have focused on quantifying systematic uncertainties associated with lens mass modeling, particularly those related to radial mass-profile assumptions and the mass-sheet degeneracy (MSD). When increased flexibility in the lens mass profile is allowed and stellar kinematics are incorporated with conservative priors, the inferred constraints broaden to  $H_0 = 67.4^{+4.1}_{-3.2} \text{ km s}^{-1} \text{ Mpc}^{-1}$  for the same lens sample (Birrer et al. 2020), illustrating the sensitivity of time-delay cosmography to internal mass degeneracies (e.g., Schneider & Sluse 2013). An updated blind analysis including improved kinematic data and high-resolution imaging yields intermediate values, such as  $H_0 = 72.1^{+4.0}_{-3.7} \text{ km s}^{-1} \text{ Mpc}^{-1}$ , albeit with enlarged uncertainties reflecting a more conservative treatment of lens-model systematics (Tdcosmo Collaboration et al. 2025). These results demonstrate that while strong-lensing time-delay cosmography provides competitive constraints on  $H_0$ , accurate modeling of the lens mass distribution remains a critical requirement for achieving reliable and precise measurements.

The need for accurate modeling of lens mass distributions in gravitational lensing studies is crucial for obtaining reliable  $H_0$  measurements. Standard models for lens galaxies often assume a power-law radial mass profile (approximately isothermal), but more physically motivated models may be necessary to account for complex processes such as baryonic feedback or self-interacting dark matter (SIDM). SIDM simulations predict that dark matter halos can develop flat-density cores, rather than the steep cusps of cold dark matter (CDM) halos, especially in the central regions of galaxies (Tulin & Yu 2018; Kaplinghat et al. 2016). Such core formation (and potential core collapse at later times) can alter the inner mass profile and, in principle, affect lensing observables.

Strong gravitational lensing provides one of the few direct probes of the total mass distribution on kiloparsec and sub-kiloparsec scales, because the positions, flux ratios, and relative time delays of multiple images depend sensitively on the projected lens potential (Sonnenfeld & Cautun 2021; Vegetti et al. 2024). In particular, the presence or absence of a highly de-magnified central image in quad or double lens systems offers a unique constraint on the inner mass profile: a steep, cuspy central profile tends to suppress the central image below detectability, whereas a shallower or cored profile can allow such a central image to be brighter and potentially observable (Quinn et al. 2016; Perera et al. 2023). Consequently, deep imaging and sensitive radio/mm observations aimed at detecting, or placing stringent upper limits on, demagnified central images have been used in a number of studies to constrain the central density slopes and core sizes of lens galaxies (e.g., Keeton 2003; Quinn et al. 2016; Wong et al. 2015; Muller et al. 2020). These constraints, in combination with stellar kinematics and lensing data, strengthen the ability to break degeneracies in the inner profile and thus refine cosmological inferences (Treu & Koopmans 2004). Recent lens modeling studies have further explored the impact of SIDM on strong lenses (Gilman et al. 2021a, 2023). For instance, Gilman et al. (2021b) demonstrated that flux-ratio anomalies in quadruply imaged quasars could constrain SIDM substructure properties, complementing constraints from dwarf galaxies and clusters. In general, lens models that allow for deviations from a simple power law—such as a core or a radial profile break—provide a route to testing whether the inner mass distribution of lens galaxies is consistent with CDM predictions or hints at SIDM-induced cores.

In this work, we incorporate the broken power law mass profile (BPL, introduced by Du et al. 2020, 2023) into lens modeling, allowing for a transition in the radial slope of the density profile. This transition can mimic a core in the inner regions of the lens galaxy. The BPL model offers greater flexibility than the elliptical power law model (EPL, introduced by Barkana 1998; Tessore & Metcalf 2015) and can phenomenologically reproduce total mass distributions that resemble those predicted in some SIDM scenarios. While the BPL model shares similarities with the cored NFW profile (Navarro et al. 1997; Tran et al. 2024), particularly in its ability to describe a central core-like structure, it provides additional flexibility in its radial slope. This flexibility allows the BPL model to capture a broader range of behaviors, from SIDM-like profiles with flat-density cores to the steep gradients typical of CDM halos. As a result, the BPL model serves as a phenomenological and versatile framework for lens modeling, suitable for exploring both SIDM-like core structures and more traditional CDM-like mass distributions. We integrate the BPL model into LENSTRONOMY (Birrer & Amara 2018) and develop a numerical solver for time delays, as an analytic Fermat potential is not available in closed form. In Sects. 2, we summarize the BPL and EPL mass models and key lensing quantities. Sects. 3 validate our approach using mock lensing data, while Sects. 4 test the BPL model with simulated data. In Sects. 5, we apply the method to real data of WGD 2038–4008, comparing BPL and EPL model fits. Finally, in Sects. 6, we discuss the implications for  $H_0$  inferences and lens model systematics. In Sects. 7 we give more detailed explanation to the differences between EPL and BPL.

## 2 LENS MASS MODELS

This section summarizes the BPL and EPL mass models for gravitational lenses. The BPL profile (Du et al. 2020) provides a flexible framework for describing galaxies with central density shallowness or cores, while the EPL model (Barkana 1998; Tessore & Metcalf 2015) emerges as a special case. All expressions assume an elliptical coordinate defined by the elliptical radius  $R_{\text{el}} = \sqrt{qx^2 + y^2/q}$  (with  $q$  the axis ratio) and  $z = x + iy$ , ensuring a consistent comparison between models. Key lensing quantities—convergence  $\kappa$ , mean convergence  $\bar{\kappa}$ , deflection angle  $\alpha$ , and deflection potential  $\psi$ —are outlined below for each model, as discussed in Sects. 2.1, 2.2, and 2.3.

### 2.1 Mass Profiles

The BPL mass density profile is defined piecewise with an inner slope  $\alpha_c$  and outer slope  $\alpha$  (with  $\alpha_c < \alpha$  for a core-like center):

$$\kappa(R_{\text{el}}) = \begin{cases} \left(\frac{b}{R_{\text{el}}}\right)^{\alpha-1} \left[ \frac{3-\alpha}{2} - \frac{3-\alpha}{\mathcal{B}(\alpha)} \mathcal{H}\left(\alpha_c, \alpha, \frac{R_{\text{el}}}{r_c}\right) \right], & R_{\text{el}} \leq r_c, \\ \frac{3-\alpha}{2} \left(\frac{b}{R_{\text{el}}}\right)^{\alpha-1}, & R_{\text{el}} > r_c, \end{cases} \quad (1)$$

where  $\mathcal{B}(\alpha) = \sqrt{\pi} \Gamma\left(\frac{\alpha-1}{2}\right) / \Gamma\left(\frac{\alpha}{2}\right)$ , and  $\mathcal{H}(\alpha_c, \alpha, \tilde{z}) = \tilde{z} \left[ {}_2F_1\left(\frac{\alpha_c}{2}, 1; \frac{3}{2}; \tilde{z}^2\right) - {}_2F_1\left(\frac{\alpha}{2}, 1; \frac{3}{2}; \tilde{z}^2\right) \right]$  with  $\tilde{z} = \sqrt{1 - R_{\text{el}}^2/r_c^2}$  (here  ${}_2F_1$  is the Gaussian hypergeometric function). The parameter  $b$  is a normalization related to the Einstein radius of the lens. The more familiar EPL profile is recovered when  $\alpha_c = \alpha$  or  $r_c \rightarrow 0$ , which yields

$$\kappa_{\text{EPL}}(R_{\text{el}}) = \frac{3-\alpha}{2} \left(\frac{b}{R_{\text{el}}}\right)^{\alpha-1}, \quad (2)$$

i.e., a single power-law surface density profile (Tessore & Metcalf 2015). In that limit, the inner correction term  $\mathcal{H}$  vanishes and  $b$  directly corresponds to the Einstein radius  $R_{\text{ein}}$ .

The mean convergence within radius  $R_{\text{el}}$  for the BPL model can be derived by integrating  $\kappa$ . While the full expression is lengthy (Du et al. 2020), an illustrative form is:

$$\bar{\kappa}(< R_{\text{el}}) = \frac{1}{\pi R_{\text{el}}^2} \int_0^{2\pi} \int_0^{R_{\text{el}}} \kappa(R') R' dR' d\theta, \quad (3)$$

which yields, for  $R_{\text{el}} \leq r_c$ ,

$$\bar{\kappa} = \left( \frac{b}{R_{\text{el}}} \right)^{\alpha-1} + \frac{m_0}{\pi \Sigma_{\text{crit}} R_{\text{el}}^2} + \frac{2}{3} \frac{3-\alpha}{\mathcal{B}(\alpha)} \left( \frac{b}{r_c} \right)^{\alpha-1} \mathcal{G} \left( \alpha_c, \alpha, \frac{R_{\text{el}}}{r_c} \right), \quad (4)$$

where  $\Sigma_{\text{crit}}$  is the critical surface density and  $m_0$  represents a central mass deficit (if  $\alpha_c < \alpha$ ) or surplus (if  $\alpha_c > \alpha$ ) compared to the extrapolated outer profile. The function  $\mathcal{G}(\alpha_c, \alpha, \tilde{z}) = \tilde{z}^3 \left[ {}_2F_1 \left( \frac{\alpha}{2}, 1; \frac{5}{2}; \tilde{z}^2 \right) - {}_2F_1 \left( \frac{\alpha_c}{2}, 1; \frac{5}{2}; \tilde{z}^2 \right) \right]$ . For  $R_{\text{el}} > r_c$ , the last term of  $\bar{\kappa}$  vanishes. In the EPL limit, only the first term remains.

The deflection angle (expressed as a complex quantity  $\alpha^* = \alpha_x - i\alpha_y$ ) for the BPL model can be written as  $\alpha^*(z) = \alpha_1^*(z) + \alpha_2^*(z)$ , where the first term  $\alpha_1^*$  corresponds to the power-law and the second term  $\alpha_2^*$  is an inner ‘‘compensation’’ term due to the break:

$$\alpha_1^*(z) = \frac{R_{\text{el}}^2}{z} \left( \frac{b}{R_{\text{el}}} \right)^{\alpha-1} {}_2F_1 \left( \frac{1}{2}, \frac{3-\alpha}{2}; \frac{5-\alpha}{2}; \zeta^2 R_{\text{el}}^2 \right), \quad (5)$$

with  $\zeta^2 \equiv (q^{-1} - q)/z^2$ , and

$$\begin{aligned} \alpha_2^*(z) = & \frac{r_c^2}{z} \frac{3-\alpha}{\mathcal{B}(\alpha)} \left( \frac{b}{r_c} \right)^{\alpha-1} \\ & \times \left[ \frac{2}{3-\alpha_c} {}_3F_2 \left( \frac{3-\alpha_c}{2}, \frac{1}{2}, 1; \frac{5-\alpha_c}{2}, \frac{3}{2}; C \right) \right. \\ & \left. - \frac{2}{3-\alpha} {}_3F_2 \left( \frac{3-\alpha}{2}, \frac{1}{2}, 1; \frac{5-\alpha}{2}, \frac{3}{2}; C \right) - S_0 \right], \end{aligned} \quad (6)$$

where  $C = r_c^2 \zeta^2$ ,  ${}_3F_2$  is a generalized hypergeometric function, and  $S_0$  is a rapidly convergent series (see Du et al. 2020 for full definitions). The EPL deflection is recovered by taking  $\alpha_c = \alpha$  (so  $\alpha_2^* \rightarrow 0$ ) and performing the coordinate transformation for an elliptical power-law potential:

$$\alpha_{\text{EPL}}^*(z) = \frac{2b}{1+q} \left( \frac{b}{R_{\text{el}}} \right)^{\alpha-1} e^{-i\varphi} {}_2F_1 \left( 1, \frac{\alpha}{2}; 2 - \frac{\alpha}{2}; -\frac{1-q}{1+q} e^{-2i\varphi} \right), \quad (7)$$

with  $\varphi = \arctan(qx, y)$  the angular coordinate in the lens plane (Tessore & Metcalf 2015). We have verified that  $\alpha_1^*$  for the BPL matches  $\alpha_{\text{EPL}}^*$  when  $\alpha_c = \alpha$ , as expected.

## 2.2 Numerical Potential Integration

While deflection angles can be obtained in closed form (in terms of special functions) for the BPL, the deflection potential  $\psi(\mathbf{x})$  generally requires integration of the deflection field. We reconstruct  $\psi$  by numerically integrating  $\alpha(\mathbf{x})$  over the image plane, following the approach of Keeton (2001). For completeness, we outline the integration procedure in an elliptical coordinate system.

We adopt coordinates  $(x, y)$  aligned with the lens principal axes, and define an elliptical radius

$$\xi^2 = qx^2 + \frac{y^2}{q}, \quad (8)$$

which differs from  $R_{\text{el}}^2$  by a constant factor for fixed  $\xi$ . We introduce a parameter  $u \in [0, 1]$  such that

$$\xi(u)^2 = u \left( qx^2 + \frac{y^2}{1 - (1 - q^2)u} \right), \quad (9)$$

which smoothly interpolates  $\xi$  from 0 to  $\infty$  as  $u$  goes from 0 to 1 (see Schramm 1990). Via 2D Green function method, the surface mass density can be expressed as  $\kappa(\xi)$  and the potential at  $\mathbf{x}$  is

$$\psi(\mathbf{x}) = \frac{1}{\pi} \int \kappa(\xi(\mathbf{y})) \ln |\mathbf{x} - \mathbf{y}| d^2y. \quad (10)$$

Performing the angular average and changing variables from area element  $d^2y$  to  $du$ , one obtains

$$\psi(x, y) = \frac{1}{2} \int_0^1 \frac{\xi(u)}{u \sqrt{1 - (1 - q^2)u}} \phi_r(\xi(u)) du, \quad (11)$$

where

$$\phi_r(\xi) = \frac{2}{\xi} \int_0^\xi s \kappa(s) ds \quad (12)$$

is the circularly symmetric potential for surface density  $\kappa(s)$  evaluated at  $\xi$ . We compute  $\phi_r(\xi)$  for the BPL profile by integrating the  $\kappa(R_{\text{el}})$  expression (treating  $\xi \approx R_{\text{el}}$  for the circular case), and then perform the  $u$ -integration numerically. The result is the deflection potential  $\psi(x, y)$  up to an arbitrary additive constant (which does not affect relative time delays).

We verified this integration procedure by applying it to the EPL model, for which  $\psi_{\text{EPL}}(x, y)$  is known analytically. Specifically, for an elliptical power-law lens one has  $\psi_{\text{EPL}}(\mathbf{x}) = \frac{1}{2-\alpha} (x\alpha_x + y\alpha_y)$  (Tessore & Metcalf 2015).

## 2.3 Validation of Fermat Potential Solver

Theoretically, the integration method described above should be applicable to any mass profile with elliptical symmetry. We first validate our numerical deflection potential solver using the EPL model, which has an analytic form for  $\psi$ . To test our method, we compute Fermat potential values on a grid in the image plane both analytically and via numerical integration, then compare the two. The fractional difference at each grid point is given by:

$$\text{Res}(x, y) = \frac{|\psi_{\text{int}}(x, y) - \psi_{\text{ana}}(x, y)|}{|\psi_{\text{ana}}(x, y)|}, \quad (13)$$

where  $\psi_{\text{int}}$  is the integrated potential and  $\psi_{\text{ana}}$  is the exact solution.

Fig. 1 shows a map of the residuals for an example power-law lens (with parameters  $\theta_E = 1''.5$ ,  $\alpha = 1.9$ ,  $q = 0.8$ , oriented along the axes). The residuals are  $\lesssim 10^{-12}$  without systematic pattern, confirming that the integration yields the correct potential to machine precision. This level of accuracy far exceeds the requirements for time-delay calculations, which depend on potential differences between image points. Moreover, evaluating  $\psi$  at a few image positions, rather than over a full grid, is highly efficient. We conclude that our numerical approach to computing the Fermat potential is both accurate and efficient, and will be used to evaluate time delays for lenses modeled with the BPL profile.

## 3 TIME DELAY AND MASS-SHEET DEGENERACY

This section introduces the time-delay relation for gravitational lenses and discusses the impact of the MSD on time-delay measurements.

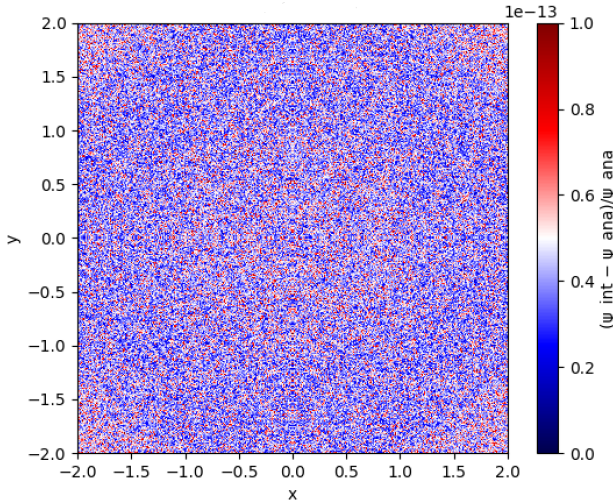


**Figure 1.** Relative residual between the numerically integrated lens potential and the analytic solution, for an EPL model. We show the relative residual  $\text{Res}(x, y)$  across the image plane for a test lens (Einstein radius  $\theta_E = 1.5''$ , slope  $\alpha = 1.9$ , axis ratio  $q = 0.8$ ). The residuals are below  $10^{-12}$  everywhere, demonstrating the high accuracy of the integration scheme.

The time-delay difference between two images in a gravitational lens system depends on the mass distribution, the deflector's geometry, and the cosmological parameters, as described in Sect. 3.1. To constrain the degeneracy and improve the precision of Hubble constant measurements, we incorporate stellar kinematics and external convergence measurements into the lens model, as outlined in Sects. 3.2 and 3.3.

### 3.1 From Time Delay to Hubble Constant

The time delay  $\Delta t_{XY}$  between the arrival times of photons corresponding to images X and Y is given by the following expression:

$$\Delta t_{XY} = \frac{D_{\Delta t}}{c} (\phi(\theta_X) - \phi(\theta_Y)), \quad (14)$$

where  $D_{\Delta t}$  is the time-delay distance,  $c$  is the speed of light, and  $\phi(\theta)$  is the Fermat potential, defined as:

$$\phi(\theta) = \frac{1}{2} |\theta - \beta|^2 - \psi(\theta), \quad (15)$$

with  $\theta$  being the angular position of the image,  $\beta$  the angular position of the source, and  $\psi(\theta)$  the lens potential.

The time-delay distance  $D_{\Delta t}$  is related to the Hubble constant  $H_0$  by the relation:

$$D_{\Delta t} \propto H_0^{-1}. \quad (16)$$

Thus, time delays can be used to measure  $H_0$  by determining the time-delay distance, which is inversely proportional to  $H_0$ .

### 3.2 Mass-Sheet Degeneracy

The imaging observables of the lensing phenomenon—such as the image positions and flux ratios<sup>1</sup>—remain invariant under the transformation known as the mass-sheet transformation (MST) (Falco

<sup>1</sup> The absolute flux value is affected by the MST.

et al. 1985), which rescales the convergence as:

$$\kappa(\theta) \rightarrow \kappa_{\lambda}(\theta) = \lambda \kappa(\theta) + 1 - \lambda, \quad (17)$$

where  $\lambda$  is a rescaling factor.

We can decompose the total mass convergence  $\kappa_{\text{true}}$  into two components: the central deflector's convergence  $\kappa_{\text{cen}}$  and the external convergence  $\kappa_{\text{ext}}$ , which arises from the mass distribution along the line-of-sight (LOS). The true convergence is then:

$$\kappa_{\text{true}} = \kappa_{\text{cen}} + \kappa_{\text{ext}}. \quad (18)$$

The model convergence  $\kappa_{\text{model}}$  is related to the true convergence  $\kappa_{\text{true}}$  by the mass-sheet transformation as (Birrer et al. 2016):

$$\kappa_{\text{model}} = \frac{\kappa_{\text{true}} - \kappa_{\text{ext}}}{1 - \kappa_{\text{ext}}}. \quad (19)$$

However, the lens model  $\kappa_{\text{model}}$  that we actually constrain can be an internal MST of  $\kappa_{\text{model}}$ , as:

$$\kappa'_{\text{model}} = \lambda_{\text{int}} \kappa_{\text{model}} + 1 - \lambda_{\text{int}}, \quad (20)$$

where  $\lambda_{\text{int}}$  is the internal rescaling factor. This equation shows that the lens model we constrain can differ from the true convergence by an internal rescaling factor  $\lambda_{\text{int}}$ . The physical meaning of the internal mass sheet is originated from the cored profile of the main lenses (e.g., Schneider & Sluse 2013; Chen et al. 2021; Blum et al. 2020). For internal mass-sheet degeneracy, the true mass distribution  $\kappa_{\text{true}}$  is then related to the internally rescaled model mass distribution  $\kappa_{\text{model}}$  as:

$$\kappa_{\text{true}} = (1 - \kappa_{\text{ext}})[\lambda_{\text{int}} \kappa_{\text{model}} + 1 - \lambda_{\text{int}}] + \kappa_{\text{ext}}. \quad (21)$$

Luckily, it can be determined by fitting the model to other constraints, such as stellar kinematics.

This equation shows how the true convergence  $\kappa_{\text{true}}$  can be recovered from the model convergence  $\kappa_{\text{model}}$  by using the external convergence  $\kappa_{\text{ext}}$  and the internal scaling factor  $\lambda_{\text{int}}$ . Importantly, when  $\kappa_{\text{ext}}$  is independently known, the lens model can be corrected by inverting the MST. However, if  $\kappa_{\text{ext}}$  is not known, this introduces a degeneracy in the time delay and other lensing observables.

The time delay is rescaled with respect to the mass-sheet transformation as:

$$\Delta t \rightarrow \Delta t' = \Lambda_{\text{tot}} \Delta t. \quad (22)$$

In the presence of both internal and external rescaling, the true time delay is related to the model time delay  $\Delta t_{\text{model}}$  by:

$$\Delta t_{\text{true}} = \Lambda_{\text{tot}} \Delta t_{\text{model}} = (1 - \kappa_{\text{ext}}) \lambda_{\text{int}} \Delta t_{\text{model}}. \quad (23)$$

Thus, to constrain the degeneracy, it is crucial to obtain additional constraints, such as stellar kinematics, which allow us to estimate  $\lambda_{\text{int}}$  and LoS weak lensing or galaxy number counts to estimate  $\kappa_{\text{ext}}$ . By incorporating these extra measurements, the degeneracy can be broken, and the true mass distribution, including the correct time delay, can be determined.

### 3.3 Kinematics Analysis

The stellar velocity dispersion,  $\sigma_{\text{los}}$ , constrains the mass distribution of the deflector galaxy. The kinematics are governed by the Jeans equation:

$$\frac{d}{dr} \left( l(r) \sigma_r(r)^2 \right) + 2\beta_{\text{ani}}(r) \frac{l(r) \sigma_r(r)^2}{r} = -l(r) \frac{d\Phi(r)}{dr}, \quad (24)$$

where  $l(r)$  is the 3D luminosity density,  $\sigma_r(r)$  is the radial velocity dispersion, and  $\beta_{\text{ani}}(r) = r^2/(r^2 + r_{\text{ani}}^2)$  is the Osipkov-Merritt (OM) anisotropy parameter (Osipkov 1979; Merritt 1985).

The observable line-of-sight velocity dispersion,  $\sigma_{\text{los}}(R)$ , is related to the 3D velocity dispersion by:

$$\sigma_{\text{los}}^2(R) = \frac{2G}{I(R)} \int_R^\infty K_\beta \left( \frac{r}{R} \right) I(r) M(r) \frac{dr}{r}, \quad (25)$$

where  $I(R)$  is the surface brightness,  $K_\beta$  is a function of  $\beta_{\text{ani}}$ , and  $M(r)$  is the 3D enclosed mass (Mamon & Łokas 2005). The corresponding form of  $K_\beta$  ( $u \equiv r/R$ ) is:

$$K_\beta = \frac{u_{\text{ani}}^2 + 1/2}{(u_{\text{ani}} + 1)^{3/2}} \left( \frac{u^2 + u_{\text{ani}}^2}{u} \right) \tan^{-1} \left( \sqrt{\frac{u^2 - 1}{u_{\text{ani}}^2 + 1}} \right) - \frac{1/2}{u_{\text{ani}}^2 + 1} \sqrt{1 - \frac{1}{u^2}}, \quad (26)$$

where  $u_{\text{ani}} = r_{\text{ani}}/R$ . The observed aperture-averaged velocity dispersion is:

$$\sigma_{\text{ap}}^2 = \frac{\int_{\text{ap}} [I(R) \sigma_{\text{los}}^2(R)] * \mathcal{S} dx dy}{\int_{\text{ap}} I(R) * \mathcal{S} dx dy}, \quad (27)$$

where  $*\mathcal{S}$  denotes convolution with the point spread function (PSF). The lens-model-predicted LOS velocity dispersion is:

$$\sigma_{\text{ap,model}}^2 = \frac{D_s}{D_{\text{ds}}} c^2 J(\xi_{\text{lens}}, \xi_{\text{light}}, \beta_{\text{ani}}). \quad (28)$$

Finally, accounting for internal and external mass-sheet transformations:

$$\sigma_{\text{ap,true}}^2 = (1 - \kappa_{\text{ext}}) \lambda_{\text{int}} \sigma_{\text{ap,model}}^2. \quad (29)$$

This rescaling constrains the MSD by matching the observed and model-predicted velocity dispersions. By measuring the velocity dispersion and external convergence, we can correct the time delay for the MST and recover the true mass distribution, leading to unbiased cosmological measurements, including the Hubble constant.

## 4 MODEL TESTS ON SIMULATED LENSES

We now assess the performance of the BPL model using simulated lens systems. Our objectives are twofold: (i) to evaluate if fitting a lens with a true BPL profile using an EPL model introduces biases in image-only modeling, as discussed in Sect. 4.1, and (ii) to confirm that fitting a BPL model to BPL-simulated data accurately recovers the input parameters, as outlined in Sect. 4.2, thus validating our implementation. These tests will provide insight into the potential systematic errors introduced when a simplified mass model, such as the EPL, is used for lenses with a steeper inner density slope.

### 4.1 EPL fits to BPL-simulated data

First, we simulate lensing data from a BPL mass model and fit it using a standard EPL model. We choose BPL parameters informed by cores discussed in Du et al. (2020). Specifically, we take an outer slope  $\alpha = 2.0$  (nearly isothermal), an inner slope  $\alpha_c = 0.5$  (significantly flattened core), and a break radius  $r_c = 0''.5$ . We set the axis ratio  $q = 0.8$ . To isolate the effect, we set the external shear to zero in this test. We then generate a mock lens image with a quadruply imaged background point source plus extended host galaxy emission, adding a smooth lens light profile. In both the simulation and the fitting, we adopt a common, idealized Gaussian PSF with a full width at half maximum (FWHM) of  $0''.1$ .

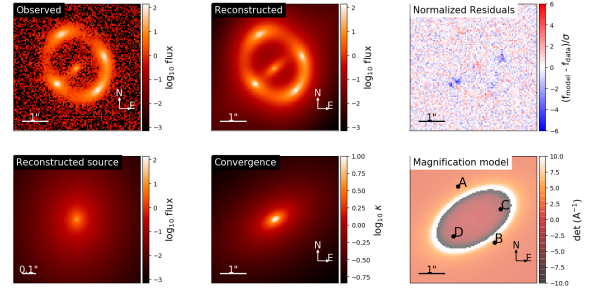


**Figure 2.** Validation test: Fitting EPL model to the BPL mock data. *Top Left:* Simulated data with four quasar images and host galaxy arcs. *Top Middle:* Best-fitting EPL model reconstruction. *Top Right:* Normalized residuals. *Bottom Left:* Reconstructed source in the source plane. *Bottom Middle:* Convergence map of the best-fit EPL model, showing an elliptical mass distribution. *Bottom Right:* Magnification map with the four quasar image positions (A–D) labeled. We assume an idealized Gaussian PSF with FWHM =  $0''.1$  in both the simulation and the fitting.

We fit the mock data with an EPL mass distribution, jointly modeling the lens galaxy light (Sérsic profile), the lensed point source, and the extended host arcs (Sérsic profile). The results are shown in Fig. 2. Even with lens light included, the EPL model failed to fully reproduce the lensed host arcs: coherent residuals remain near the image positions. This behavior is expected because the true mass distribution contains a core (shallower central  $\kappa$ ), whereas the single-power-law EPL compensates by adjusting its global slope and ellipticity. We also note that the bright lens galaxy, overlapping the faint host, can partially mask mass-model deficiencies: the fitting algorithm may absorb some flux mismatches into the lens-light component. Consequently, relatively small residuals at the point-image locations should not be over-interpreted as evidence for an adequate mass model—the light model can soak up discrepancies that originate in the mass profile.

### 4.2 BPL fits to BPL-simulated data

Next, to verify the internal consistency of our BPL implementation, we simulate lens data using a BPL model and then fit it with the same functional form. We use the same parameters as above (outer slope  $\alpha = 2.0$ , inner  $\alpha_c = 0.5$ ,  $r_c = 0.5$ , etc.) to generate mock images, and then run our BPL fitting pipeline. As shown in Fig. 3, the BPL model provides an excellent fit to the data, with residuals consistent with noise. The recovered mass parameters are within the statistical uncertainties of the true input values. This confirms that: (i) the simulation and fitting procedures are properly coded and inverses of each other, and (ii) the BPL model is flexible enough to capture the lensing observables when it is indeed the correct model.

These simulation tests are designed to validate the internal consistency of our imaging-modeling implementation and to illustrate the impact of mass-model mismatch in recovering the lens mass distribution from imaging data. Accordingly, any differences in the predicted time delays discussed later are most naturally interpreted as arising, at least in part, from how such mass-model mismatch propagates into the Fermat potential.

## 5 LENS MODELING OF WGD 2038–4008

We now apply our modeling approach to the quadruply imaged quasar WGD 2038–4008. This system was discovered in the Dark Energy

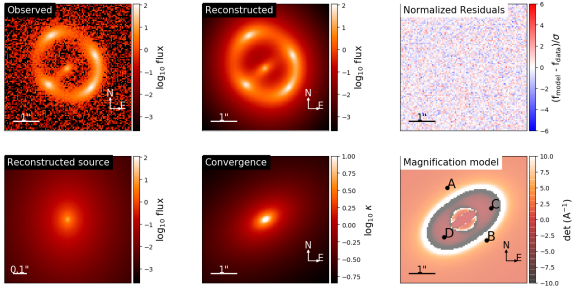


**Figure 3.** Validation test: Fitting BPL model to the BPL mock data. Panels are analogous to Fig. 2. The BPL model successfully reproduces the lensed images and arcs, yielding negligible residuals. The input and recovered mass profile parameters agree within uncertainties.

Survey footprint (Agnello et al. 2018) and consists of a lens galaxy at  $z_L = 0.228$  and a background quasar at  $z_s = 0.777$  (Buckley-Geer et al. 2020). It has four resolved quasar images (labeled A–D) and faint host galaxy arcs visible in deep imaging. Crucially, a stellar velocity dispersion of  $296 \pm 19 \text{ km s}^{-1}$  (aperture size  $0''.75 \times 1''.0$ , seeing  $0''.9$ ) has been measured for the lens galaxy using Gemini/GMOS-S spectroscopy (Buckley-Geer et al. 2020), providing an additional constraint for our mass models. This data set makes WGD 2038–4008 an excellent candidate for time-delay cosmography. The choice of this lens system is motivated by the fact that, in previous fits, the system has shown potential for a central imaging feature (Shajib et al. 2019, 2022).

Our modeling procedure closely follows that of recent lensing analyses (e.g., Wong et al. 2020; Shajib et al. 2020). We describe the imaging data and preparation in Sect. 5.1, then define two model settings in Sect. 5.2. We perform Bayesian inference for each family, including an exploration of model systematics and a model averaging procedure in Sect. 5.3. Finally, in Sect. 5.4, we combine stellar kinematics and external convergence to refine the lens model and constrain the mass-sheet factor, enabling more precise time-delay predictions and cosmological inferences.

### 5.1 Data and Preprocessing

We use *HST* imaging of WGD 2038–4008 from the WFC3 camera in three filters: F160W (near-infrared), F814W (optical *I*-band), and F475X (blue). Each filter has four dithered exposures (total exposure times of 2280 s in F160W, 2400 s in F814W, 2268 s in F475X), which we retrieved from the Mikulski Archive for Space Telescopes. The data were processed with standard DRIZZLEPAC routines to produce combined images in each band with a pixel scale of  $0''.08$  for WFC3/IR and  $0''.04$  for WFC3/UVIS, respectively. We constructed empirical PSFs for each band by stacking 4–6 unsaturated stars in the field, and then iteratively refined the PSF models using the quasar image residuals (e.g., following Chen & et al. 2016). The images were astrometrically aligned to sub-pixel precision using common sources across the bands. A similar image download and preprocessing procedure, from which our pipeline draws inspiration, can be found in Tan et al. (2024)<sup>2</sup>, although it was not specifically designed for this target.

Fig. 4 shows a false-color composite of the system. The four quasar images (A–D) form a classic fold/cusp configuration around the lens galaxy. The quasar is relatively red, appearing brightest in F160W;

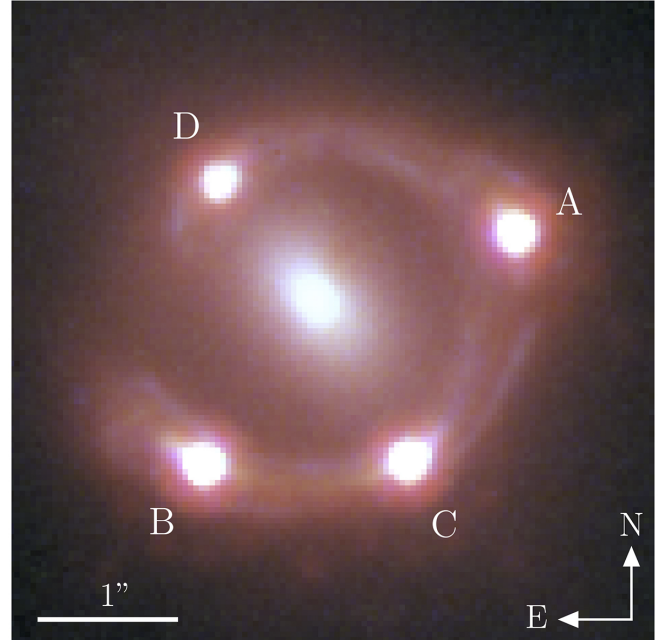


**Figure 4.** Color composite of WGD 2038–4008 from *HST* WFC3 imaging (F160W in red, F814W in green, F475X in blue). The four quasar images A, B, C, D surround the foreground lens galaxy (center). Extended lensed host galaxy features are visible as faint greenish arcs. North is up and east is left; the image cutout is  $5''$  on a side.

the extended host galaxy is detected mainly in F160W and F814W (as greenish arcs), with marginal signal in F475X. We mask out neighboring objects and regions without detected lensing signal when fitting the pixel data. Because the quasar images saturate the core of the PSF in the long F160W exposures, we use smaller stamps around each quasar to locally correct any saturation effects (these corrections are  $\lesssim 0.05$  mag and have negligible impact on modeling). We adopt a multi-scale noise model: background sky variance is taken from data in object-free regions and checked against the weight maps, and we add an estimated 1% flux uncertainty for each quasar image to account for PSF modeling errors. These choices ensure that the reduced  $\chi^2$  of the best models is close to 1 in each band, indicating a statistically adequate fit.

### 5.2 Model Settings and Priors

We model the lens with two closely related mass-profile families—EPL(PEMD model) and BPL—as discussed and compared above, while keeping the deflector light model fixed to the deflector configuration, so that mass–light coupling and PSF handling remain fully consistent. Imaging constraints are taken from HST WFC3 F160W, F814W, and F475X. During optimization we iteratively reconstruct the PSF around the quasar images, and we restrict the image-plane likelihood to circular apertures of fixed radii  $\{2''.2, 3''.6\}$  arcsec (IR, UVIS), masking unrelated companions within these regions. Shajib et al. (2022) uses mask sizes of  $\{2''.3, 3''.7\}$ . However, we find that this choice leads to a poor BIC value. To improve model performance, we therefore adopt a smaller mask size.

Under a shared elliptical isodensity geometry, both families allow the mass centroid  $(\theta_1, \theta_2)$  to vary independently of the light centroid and include an external shear  $(\gamma_{\text{ext}}, \phi_{\text{ext}})$ . The EPL is characterized by a single Einstein radius  $\theta_E$ , an axis ratio  $q_m$  with position angle

<sup>2</sup> <https://github.com/Project-Dinos/dinos-i>

$\phi_m$ , and a single slope  $\gamma$ . The BPL retains the same  $(q_m, \phi_m)$  but replaces the single slope with an inner/outer pair  $(\alpha_c, \alpha)$  joined at a break radius  $r_c$ , thereby capturing curvature in the radial mass profile while preserving the overall ellipticity and centroid. Additionally, the BPL model includes a scale radius  $b$  corresponding to  $\theta_E$ . Because the Einstein radius of the BPL model cannot be expressed analytically, we adopt the effective Einstein radius  $\theta_E$  in this work. The effective Einstein radius is computed as the circularized radius  $\theta_E$  at which the enclosed mean convergence satisfies  $\bar{\kappa}(< \theta_E) = 1$  (i.e. defined via circular, not elliptical, apertures).

The source is reconstructed using a compact basis, where both the elliptical Sérsic and shapelets (Refregier 2003; Birrer et al. 2015) components share the same coordinate system. The reconstruction is performed jointly across multiple bands to ensure consistency. For the shapelets model, the number of shapelet modes  $n_{\max}$  is set based on the resolution requirements for each band. Specifically,  $n_{\max}$  defines the maximum order of the shapelet decomposition, controlling the number of radial and angular modes used to describe the source profile. A higher  $n_{\max}$  allows for a finer resolution but also increases the complexity of the model. For the shapelets decomposition is parametrized by the maximum order  $n_{\max}$ , with the choices  $\{n_{\max}^{IR}, n_{\max}^{UVIS}\} = \{7, 11\}, \{8, 12\}$  and  $\{9, 13\}$ . The deflector light is described by a triple Sérsic model (three Sérsic share the same coordinates) that permits colour gradients by freeing  $(I_{\text{eff}}, \theta_{\text{eff}}, n_s)$  per band while tying the centroids across bands, so that differences between EPL and BPL arise from the mass model rather than the light parameterization. The specific analytical expressions for the light profile can be found in Appendix A.

Priors are weakly informative and follow standard cosmographic practice: the mass centroid is uniform within  $\pm 0.^{\circ}2$  of the light centroid;  $\theta_E$  is uniform over a plausible interval bracketing the isophotal Einstein scale;  $q_m \in [0, 1]$  and  $\phi_m \in [0, 180^{\circ}]$ ; for EPL we take  $\gamma \in [1.5, 2.8]$ ; for BPL we adopt  $\alpha \in [1.0, 3.0]$ ,  $\alpha_c \in [0.01, 3.0]$  with a soft regularization that enforces monotonic enclosed mass and  $r_c \in [0.^{\prime\prime}04, 3.^{\prime\prime}0]$ ; for the tidal field,  $\gamma_{\text{ext}} \in [0, 0.2]$  and  $\phi_{\text{ext}} \in [0, 180^{\circ}]$ . Light parameters use broad uniforms (or weak Gaussians) that ensure positive fluxes and realistic sizes/indices.

For each model configuration, we first perform particle swarm optimization (PSO) followed by iterative PSF updates using the `psf_iteration` function in `LENSTRONOMY`. After each PSF update, we re-align the IR frame to the UVIS frame using the quasar image positions and then re-optimize the model. This process alternates between PSO and PSF iterations, ensuring the model is progressively refined. Once the initial optimization is completed, we perform MCMC with 10,000 burn-in steps followed by 10,000 MCMC steps (Run 1). Afterward, we repeat the burn-in with 10,000 steps and MCMC with 10,000 steps (Run 2) to account for the influence of the iterative PSF updates. Convergence is monitored by verifying that the walker medians and dispersions have stabilized after 1,000 steps, and the final 1,000 steps are used for posterior analysis.

The complete modelling workflow, including all testing and verification runs, accumulated a total computational cost of approximately  $10^5$  core-hours. In fact, due to the BPL model involving more complex calculations of confluent hypergeometric functions and the need for integration in the lens potential calculation, the overall computation took approximately 1/3 to 1/2 more core-hours compared to the EPL model. For the EPL model family, the overall model configuration and optimization strategy closely follow the publicly available implementation described in Shajib et al. (2022), as documented in

the accompanying GitHub repository<sup>3</sup>. This ensures that our EPL results are directly comparable to previous analyses of the same system. The full set of model configurations adopted in this work, together with the corresponding posterior samples for both the EPL and BPL families, will be made publicly available in a dedicated repository upon publication.

### 5.3 Bayesian Information Criterion

We compare different modeling configurations using the Bayesian Information Criterion (BIC). The BIC is not used here as an absolute model-selection statistic, since the imaging likelihood is evaluated over a large number of highly correlated pixels and therefore does not strictly satisfy the independence assumptions underlying the BIC. Instead, in this work the BIC is employed only as a relative weighting tool within a controlled model family (EPL or BPL separately), where all configurations share the same data set, likelihood definition, masking strategy, and PSF treatment. In this context, the role of the BIC is to stabilize the ranking of closely related model realizations against numerical fluctuations arising from finite optimization accuracy and sampling noise, rather than to provide a rigorous estimate of Bayesian evidence. Consequently, no absolute evidence comparison between the EPL and BPL model families is attempted, and the resulting weights are not interpreted as a statement of global model preference. For each MCMC chain (i.e., each modeling configuration), we compute the BIC from the maximized image-likelihood. The BIC is defined as:

$$\text{BIC} = k \ln n - 2 \ln \hat{\mathcal{L}}, \quad (30)$$

where  $n$  is the number of independent data points used by the likelihood. In our imaging case,  $n$  corresponds to the total number of unmasked pixels across all bands and exposures.  $k$  is the total number of fitted parameters (both non-linear and linear), and  $\hat{\mathcal{L}}$  is the maximum value of the image likelihood attained by the chain. We compute:

$$k = k_{\text{nonlin}} + k_{\text{lin}}, \quad (31)$$

where  $k_{\text{nonlin}}$  is the number of non-linear parameters in all model components (lens mass, source light, lens light, point sources, etc.), and  $k_{\text{lin}}$  is the number of linear amplitudes solved at each likelihood evaluation (i.e., linear light coefficients).

We calculate one BIC value for each sampling chain. Within each model family, we evaluate the relative performance of different parameter sets by computing the  $\Delta\text{BIC}$  values as

$$\Delta\text{BIC}_i = \text{BIC}_i - \min_j(\text{BIC}_j), \quad (32)$$

where both  $\text{BIC}_i$  and  $\min_j(\text{BIC}_j)$  are evaluated within the same model family, and the index  $j$  corresponds to the parameter set that yields the minimum BIC in that family. This definition allows us to measure how strongly each realization is disfavored relative to the best-fitting model of its family. And the classical BIC weights are calculated as:

$$w_i \propto \exp\left(-\frac{1}{2}\Delta\text{BIC}_i\right). \quad (33)$$

However, finite optimization and sampling introduce scatter in the BIC values. To account for this, we adopt a robust weighting scheme that marginalizes over an effective BIC noise scale. We define  $\sigma_{\text{num}}$

<sup>3</sup> <https://github.com/TDCOSMO/WGD2038-4008>

as the numerical scatter (estimated from repeated runs of identical configurations) using a robust median absolute deviation (MAD) estimator, and  $\sigma_{\text{mod}}$  as the typical inter-configuration variation (estimated from differences between adjacent configurations within a predefined neighbor graph). We estimate  $\sigma_{\text{num}}$  and  $\sigma_{\text{mod}}$  to quantify numerical noise and model differences, respectively.  $\sigma_{\text{num}}$  is computed from the absolute differences between repeated runs of the same configuration, using the MAD and scaled by a factor of 1.48 which is to convert the MAD into an approximate standard deviation, providing a more accurate estimate of the noise in the data.  $\sigma_{\text{mod}}$  is calculated from the differences between adjacent configurations' BIC values, also using MAD and scaling by 1.48. Both estimations help reduce sensitivity to small, non-physical fluctuations in BIC, ensuring robustness across different configurations and preserving the usual  $e^{-\Delta\text{BIC}/2}$  behavior in the zero-noise limit. The combined noise scale  $\sigma$  is then:

$$\sigma = \sqrt{\sigma_{\text{mod}}^2 + \sigma_{\text{num}}^2}. \quad (34)$$

For each chain  $i$ , with  $\Delta\text{BIC}_i$ , we define a latent variable  $X_i$ , distributed as a normal variable:

$$X_i \sim \mathcal{N}\left(\mu_i, \sigma^2\right), \quad \mu_i \equiv -\frac{1}{2} \Delta\text{BIC}_i. \quad (35)$$

The effective (unnormalized) weight is the expectation:

$$\tilde{w}_i = \mathbb{E}[\min(1, e^{X_i})] = \Phi\left(\frac{\mu_i}{\sigma}\right) + \exp\left(\mu_i + \frac{1}{2}\sigma^2\right) \Phi\left(\frac{-\mu_i - \sigma^2}{\sigma}\right), \quad (36)$$

where  $\Phi$  is the standard normal cumulative distribution function (CDF). The final weight is normalized by:

$$w_i = \frac{\tilde{w}_i}{\max_j \tilde{w}_j}. \quad (37)$$

This weighting scheme is not intended to redefine Bayesian evidence or to replace a full evidence-based model comparison. Instead, it is designed to stabilize the relative ranking of closely related model configurations against numerical fluctuations arising from finite optimization accuracy and sampling noise, while preserving the usual  $\exp(-\Delta\text{BIC}/2)$  behaviour in the zero-noise limit.

In practice, we compute the model-averaged parameter posterior distributions as:

$$P(\xi)_{\text{avg}} = \sum_i w_i P(\xi | \mathcal{M}_i), \quad (38)$$

where  $P(\xi | \mathcal{M}_i)$  is the posterior distribution of the parameter  $\xi$  for model  $\mathcal{M}_i$ , and  $w_i$  is the weight for each model as determined by its BIC score. This method provides a model-averaged estimate for the parameters that accounts for the relative plausibility of each model. Table 1 presents the final BIC results for each chain in both the EPL and BPL families.

#### 5.4 Combining Stellar Kinematics and External Convergence

To constrain the mass-sheet degeneracy, we combine stellar kinematics with an external convergence ( $\kappa_{\text{ext}}$ ) constraint. We first perform dynamical modeling of the deflector using Eq. 25. The luminosity density  $l(r)$  is obtained by deprojecting the F160W surface brightness profile, which yields an effective radius  $\theta_{\text{eff}} = 3.''2 \pm 0.''02$ . This profile is approximated with an elliptical multi-Gaussian expansion (MGE) (Cappellari 2002) and converted to a spherical 3D light profile under the Jeans equation assumption. A 2% uncertainty is propagated from  $\theta_{\text{eff}}$  to the MGE scales.

**Table 1.** BIC comparison for EPL and BPL models. BIC values are not to be compared across model families.

$n_{\text{max}}$	Run	$\Delta\text{BIC}$	Weight
EPL			
{9, 13}	2	0	1.00
{9, 13}	1	39	0.94
{7, 11}	2	541	0.30
{7, 11}	1	542	0.30
{8, 12}	2	640	0.22
{8, 12}	1	647	0.21
BPL			
{9, 13}	1	0	1.00
{9, 13}	2	2	1.00
{7, 11}	2	639	0.22
{7, 11}	1	650	0.21
{8, 12}	2	998	0.05
{8, 12}	1	1052	0.04

For the velocity anisotropy, we adopt a Jeffreys' prior on the scaling factor  $a_{\text{ani}}$  (where  $r_{\text{ani}} \equiv a_{\text{ani}} \theta_{\text{eff}}$ ), sampling  $\log a_{\text{ani}}$  uniformly over  $[0.5, 5] \theta_{\text{eff}}$  following Birrer et al. (2016, 2020).

The external convergence  $\kappa_{\text{ext}}$  is estimated statistically from the galaxy environment. Rather than performing a direct number count analysis, we use the precomputed  $\gamma_{\text{ext}}-\kappa_{\text{ext}}$  relation from Shajib et al. (2022) (based on Buckley-Geer et al. 2020) and sample the  $\kappa_{\text{ext}}$  distribution corresponding to the external shear posterior from our lens model.

The distance ratio  $D_s/D_{\text{ds}}$  is constrained using the Pantheon SN sample (Scolnic et al. 2018). We approximate the luminosity distance with a fourth-order Taylor expansion, select the highest-evidence model including  $j_0$  via nested sampling (Skilling 2004), and convert to angular diameter distances via  $D_A = D_L/(1+z)^2$  to obtain the  $D_s/D_{\text{ds}}$  posterior.

Finally, the internal mass normalization  $\lambda_{\text{int}}$  is treated as a free parameter and constrained through the stellar kinematics:

$$\lambda_{\text{int}} = \frac{\sigma_{\text{ap}}^2}{(1 - \kappa_{\text{ext}}) \left(\frac{D_s}{D_{\text{ds}}}\right) c^2 J(\xi_{\text{lens}}, \xi_{\text{light}}, \beta_{\text{ani}})}, \quad (39)$$

where  $\sigma_{\text{ap}}$  is the aperture velocity dispersion, and  $J(\xi_{\text{lens}}, \xi_{\text{light}}, \beta_{\text{ani}})$  is a dimensionless factor that depends only on angular quantities (lens model parameters  $\xi_{\text{lens}}$ , light distribution  $\xi_{\text{light}}$ , and OM anisotropy  $\beta_{\text{ani}}$ ) and is directly related to the model convergence  $\kappa_{\text{model}}$  (Birrer et al. 2016).

## 6 RESULTS

In this section, we present the main outcomes of our analysis of WGD 2038–4008, focusing on the comparison between the EPL and BPL mass-model families. We begin by comparing the lens model fits and derived structural parameters for the two models, including their Einstein radii, projected ellipticities, external shear, and radial slope structure Sect. 6.1. We then examine the predicted time delays based on image modeling alone under a fiducial flat  $\Lambda$ CDM cosmology Sect. 6.2. Following this, we incorporate stellar kinematic constraints and line-of-sight (LOS) external convergence to refine the time-delay predictions and obtain mass-sheet factors Sect. 6.3. Lastly, we use the BIC-weighted posteriors from the combined imaging, kinematics, and LOS analyses to construct the time-delay distance and  $H_0$

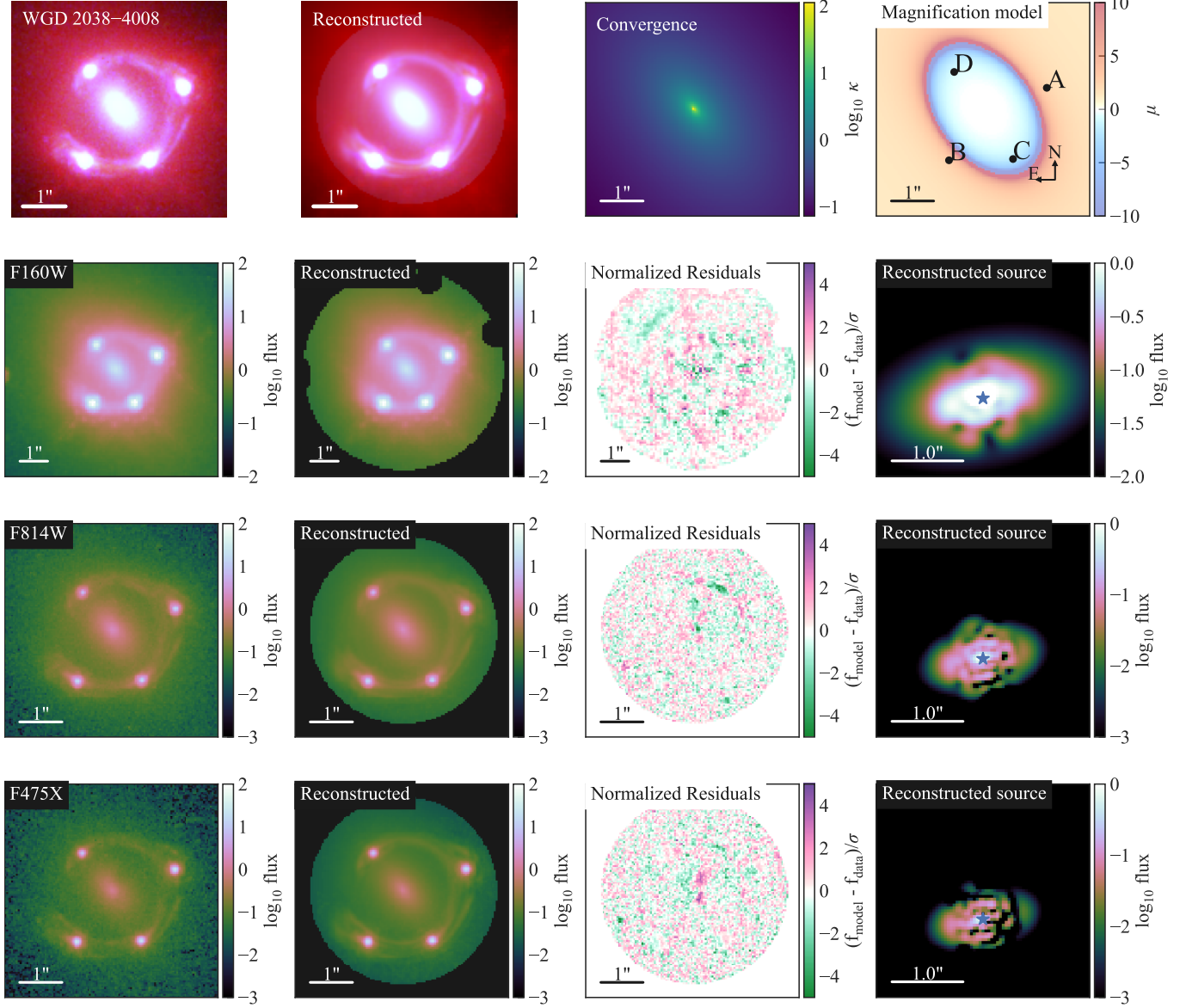


**Figure 5.** Lenstronomy-based lens model and image reconstruction of WGD 2038-4008 using an EPL mass profile. The top row shows, from left to right, the observed RGB composite, the model-predicted RGB composite, the convergence map ( $\kappa$ ), and the magnification ( $\mu$ ). Rows 2–4 display, for each HST filter, the observed image, the reconstructed image, the residual, and the reconstructed source plane: F160W (row 2), F814W (row 3), and F475X (row 4). All scale bars correspond to  $1''$ . In the source panels, the star marks the centroid of the quasar host galaxy.

posteriors, quantifying the model dependence of the cosmographic inference between the EPL and BPL families Sect. 6.4.

### 6.1 Fitting Results and Parameter Constraints

In this subsection, we present the lens model fitting results for both the EPL and BPL model families using the multi-band imaging data. Figs. 5 and 6 show the observed images, model predictions, residuals, and reconstructed source for the best-fitting models in each family. Overall, both models reproduce the observed lensed morphology and image configurations equally well. The residual patterns and reconstructed source structures are broadly similar between the two model families, and no statistically significant differences are evident at the current data quality and angular resolution. Consequently, the

imaging data alone do not provide sufficient discriminatory power to distinguish between the EPL and BPL mass profiles. Table 2 summarizes the reduced  $\chi^2$  values for the joint three-band and for each band separately (F160W, F814W, and F475X) for the best-fitting models shown in Figs. 5 and 6, indicating that the overall fit quality is statistically comparable between the two model families: the combined reduced  $\chi^2$  values differ only marginally and are similarly close to unity, while the band-by-band reduced  $\chi^2$  values differ at the  $10^{-3} \sim 10^{-2}$  level (including in F160W), with the optical bands (F814W and F475X) effectively indistinguishable.

Fig. 7 and Table 3 present the BIC-weighted posteriors for key lensing diagnostics and compare the projected mass distribution (convergence  $\kappa$ ) and magnification  $\mu$  of the EPL and BPL families. The effective Einstein radius is  $\theta_E = 1.''380 \pm 0.''001$  for EPL

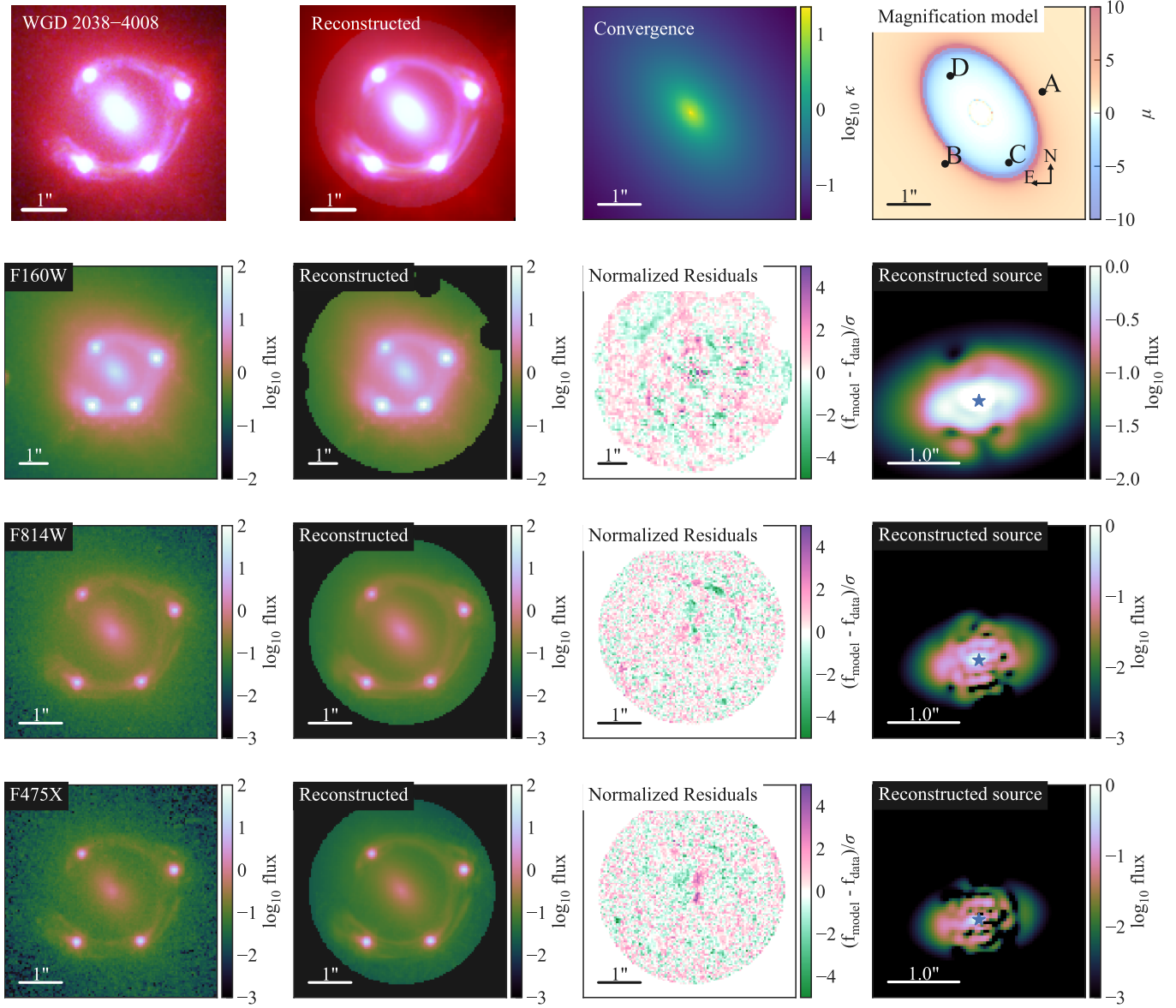


**Figure 6.** Same as Fig. 5. Lenstronomy-based lens model and image reconstruction of WGD 2038–4008 using the BPL mass profile. The magnification map exhibits a nearly circular feature near the lens centre, indicating that the central lensing geometry is primarily governed by the mass components with lower slope. In the absence of a clearly detectable central image, the strong-lensing imaging observables mainly constrain the projected mass distribution near the Einstein radius, while providing only weak sensitivity to the mass profile at radii well inside it. As a result, the inferred inner mass slope is not directly constrained by the imaging data alone, but is largely driven by the assumed functional form of the mass parameterization.

**Table 2.** Reduced  $\chi^2$  for EPL and BPL best-fitting models (shown in Figs. 5 and 6) for all the three bands combined, and for the individual bands F160W, F814W, and F475X.

Bands	BPL	EPL
Combined	0.907	0.903
F160W	0.752	0.738
F814W	0.900	0.898
F475X	1.013	1.014

and  $\theta_E = 1''.364 \pm 0''.004$  for BPL. The mass ellipticity at intermediate radii is similar, with  $q_m = 0.600 \pm 0.005$  (EPL) and  $0.650 \pm 0.02$

(BPL), i.e.,  $1 - q_m \approx 0.35 \sim 0.4$ . The inferred external shear is strongly model dependent: we find  $\gamma_{\text{ext}} = 0.077 \pm 0.004$  for the EPL family, compared to  $0.119 \pm 0.004$  for the BPL family, implying a  $\simeq 7.4\sigma$  discrepancy that far exceeds the nominal statistical uncertainties. Given the well-known degeneracies between  $\gamma_{\text{ext}}$  and other lens parameters, and its sensitivity to modelling choices (most notably PSF reconstruction), we interpret this offset as reflecting model-dependent trade-offs rather than a purely environmental measurement (Shajib et al. 2022).

The main distinction concerns the radial slope structure. The single-slope EPL corresponds to a density index  $\gamma' = 2.30 \pm 0.02$ , whereas the BPL model is consistent with a broken profile characterized by an outer slope  $\alpha = 2.799 \pm 0.066$ , an inner slope

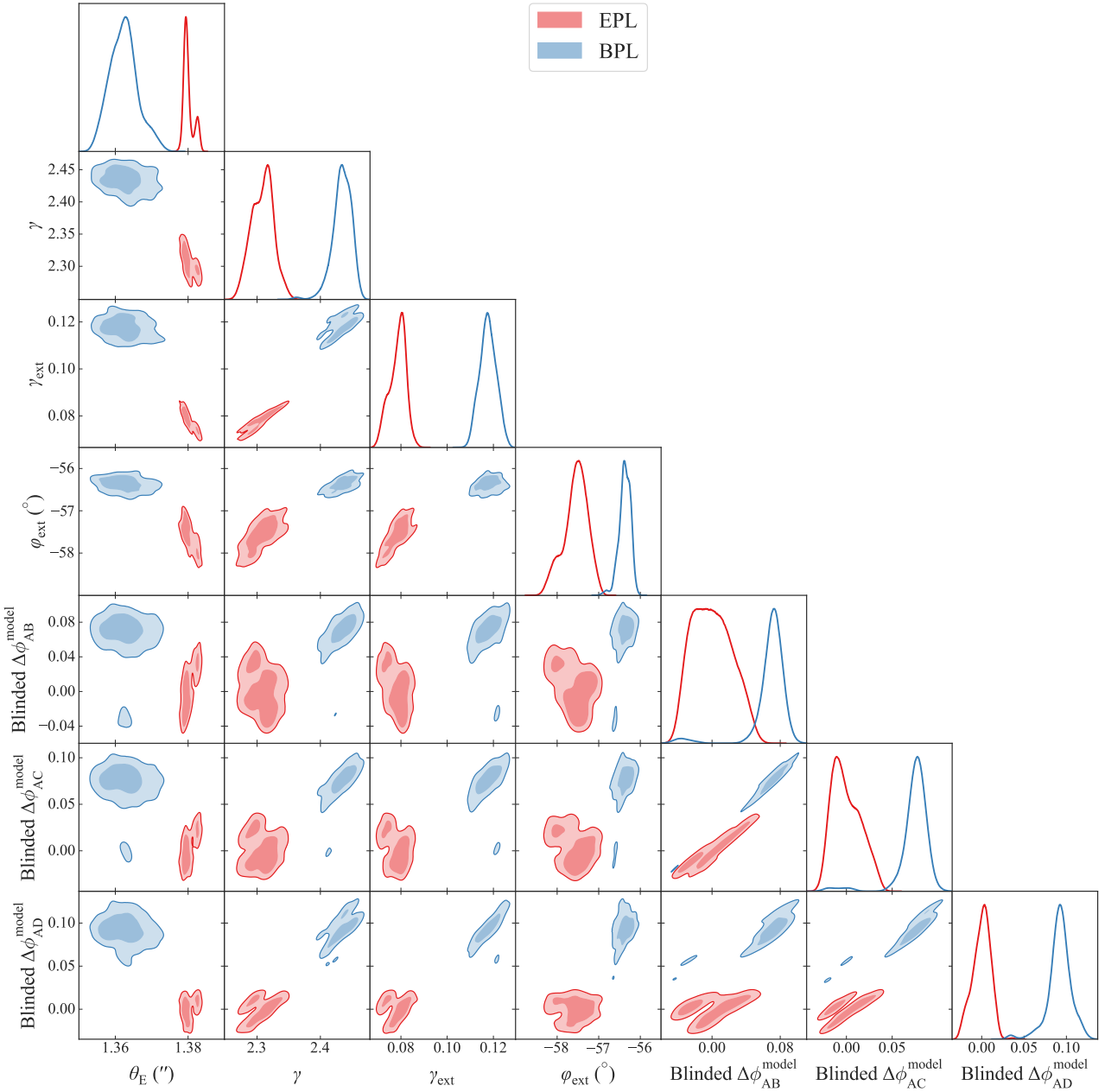


**Figure 7.** distributions of BIC weighted parameters of the EPL (red) and BPL (blue) models, specifically focusing on the effective Einstein radius  $\theta_E$ . The tangential critical curve is traced at points where the tangential eigenvalue of the lensing Jacobian equals zero. Subsequently, the area of the primary closed loop encircling the lens center is determined. The local “effective” slope is computed with  $\gamma(\theta_E) = 2 - \frac{d \ln \alpha(\theta_E)}{d r}$  where  $\alpha(\theta_E)$  is the azimuthally averaged deflection amplitude; thus  $\gamma(\theta_E)$  is a lensing-derived (2D) effective slope obtained from the deflection field (for a true power-law, it equals the usual logarithmic index). To compare the differences in Fermat-potential offsets among the image positions, we set the mean value of the EPL model’s  $\phi_{AX}$  as the zero point of the coordinate reference. Shaded bands indicate the  $1\sigma$  and  $2\sigma$  credible intervals.

$\alpha_c = 1.26 \pm 0.06$ , and a break radius  $r_c = 0.40 \pm 0.08$  arcsec. As a result, the BPL parameterization allows for a shallower inner mass distribution within  $\sim 1.2\text{--}1.8$  kpc (this is not directly constrained by imaging), while remaining steeper at larger radii. Consistent with this behaviour, the lensing-derived effective slope evaluated at the Einstein ring,  $\gamma(\theta_E)$ , is modestly steeper for the BPL model ( $2.43 \pm 0.02$ ) than for the EPL model ( $2.30 \pm 0.02$ ), reflecting that  $\theta_E$  lies closer to the outer-slope regime.

This behaviour is further illustrated by the radial profiles of the mean convergence shown in Fig. 14 (Sect. 7). While the EPL and BPL

models are tightly constrained to yield similar enclosed convergence near the Einstein radius—where strong-lensing imaging provides the strongest leverage—they exhibit different trends at smaller radii. In particular, the BPL model permits a redistribution of mass such that the inner regions ( $R \ll \theta_E$ ) are comparatively flatter, whereas the effective slope evaluated near  $\theta_E$  can be steeper. This difference arises naturally from the radial flexibility of the BPL parameterization, rather than representing a contradiction between constraints on inner and Einstein-scale mass distributions.

While the inferred BPL inner slope is qualitatively compatible

with a core-like flattening, we emphasize that, in the absence of a clearly detected central image in the current data, strong-lensing observables are primarily sensitive to the projected mass distribution near the Einstein radius and thus provide only weak constraints on the inner profile at radii  $r \ll \theta_E$ . In this regime, the inference is driven by the adopted mass parameterization and the joint lensing–dynamical modelling, rather than by lensing information alone. Overall, both model families provide comparably good fits to the data, with only subtle trade-offs in source morphology and inner-slope preference that the current observations do not decisively resolve.

Notably, the parameter results for the EPL model show some differences when compared to those obtained by (Shajib et al. 2022) using LENSTRONOMY, though they are more consistent with the results derived from the GLEE code. These differences could stem from the inherent degeneracy of the EPL model and the random nature of PSF iteration. We extended the PSF iteration process two to three times longer than in previous studies, improving the overall accuracy of the model.

## 6.2 Time-delay predictions in the image-modelling-only case

To assess the model dependence of the predicted time delays prior to including kinematics and external convergence, we compute the BIC-weighted posteriors of the EPL and BPL families under a flat  $\Lambda$ CDM cosmology with  $H_0 = 70 \text{ km s}^{-1} \text{ Mpc}^{-1}$  and  $\Omega_m = 0.3$ .

Fig. 8 shows the BIC-weighted time-delay posteriors for the AB, AC, and AD image pairs. The two mass-model families yield systematically different predictions: the BPL model systematically produces larger  $|\Delta t|$  than the EPL model across all image pairs. This behaviour reflects the different inner-density slopes of the two families, which reshape the radial mass profile and therefore modify the Fermat-potential surfaces in a coherent manner. In support of this argument, we provide a more detailed discussion based on the model posteriors in Sect. 7. We find that the dominant contribution to the time-delay difference between the EPL and BPL families arises from the geometric term. The deflection-angle variations modify the geometric path length component of the Fermat potential in a coherent manner across all image pairs, while the contribution from differences in the lens potential remains subdominant.

Quantitatively, the raw EPL and BPL predictions (i.e. without the stellar kinematics and LOS correction) are:

$$\Delta t_{AB}^{\text{EPL}} = -5.543_{-0.133}^{+0.139} \text{ days}, \quad \Delta t_{AB}^{\text{BPL}} = -5.945_{-0.063}^{+0.080} \text{ days}, \quad (40)$$

$$\Delta t_{AC}^{\text{EPL}} = -11.198_{-0.196}^{+0.165} \text{ days}, \quad \Delta t_{AC}^{\text{BPL}} = -12.085_{-0.111}^{+0.149} \text{ days}, \quad (41)$$

$$\Delta t_{AD}^{\text{EPL}} = -27.314_{-0.265}^{+0.293} \text{ days}, \quad \Delta t_{AD}^{\text{BPL}} = -29.866_{-0.336}^{+0.356} \text{ days}. \quad (42)$$

The relative time delays differ from those of the EPL model by approximately 9–16%. The offsets between the two families are therefore coherent, stable across image pairs, and directly trace the differing radial mass distributions. Since larger  $|\Delta t|$  at fixed observed delays corresponds to a smaller inferred time-delay distance  $D_{\Delta t}$ , and thus a higher inferred  $H_0$ , these discrepancies demonstrate that the choice between EPL and BPL already induces a non-negligible systematic shift at the image-modelling-only stage. This motivates treating the inner-profile uncertainty as an explicit component of the error budget in the full cosmographic analysis.

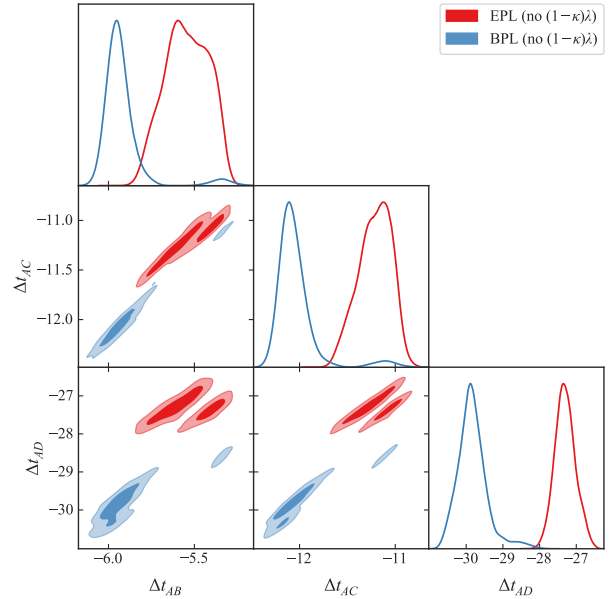


**Figure 8.** BIC-weighted predicted time-delay posteriors (uncorrected for  $(1 - \kappa_{\text{ext}})\lambda_{\text{int}}$ ) for the AB, AC, and AD image pairs under a flat  $\Lambda$ CDM cosmology with  $H_0 = 70 \text{ km s}^{-1} \text{ Mpc}^{-1}$  and  $\Omega_m = 0.3$ . The BPL (blue) model predicts consistently larger  $|\Delta t|$  than the EPL (red) model, reflecting their differing inner-density slopes.

## 6.3 Time-delay predictions combining kinematics and LOS

We refine the lens-model inferences by incorporating both the stellar kinematics and the LOS external convergence. The construction of the  $\kappa_{\text{ext}}$  prior follows the procedure described in Sect. 5.4, and the resulting distributions for the EPL and BPL families are shown in Fig. 9. The BIC-weighted posteriors yield  $\kappa_{\text{ext}}^{\text{EPL}} = 0.074 \pm 0.052$  and  $\kappa_{\text{ext}}^{\text{BPL}} = 0.162 \pm 0.063$ . This model dependence in  $\kappa_{\text{ext}}$  is predominantly inherited from the different external-shear posteriors, since each sampled  $\gamma_{\text{ext}}$  from the EPL/BPL image models is mapped to  $\kappa_{\text{ext}}$  using the same Buckley–Geer calibration (Buckley–Geer et al. 2020); any sensitivity to the inner-density slope thus enters only indirectly through its impact on the inferred  $\gamma_{\text{ext}}$ , which itself remains conditioned on the adopted lens mass model.

After applying the full mass-sheet correction  $(1 - \kappa_{\text{ext}})\lambda_{\text{int}}$  and combining all constraints, the predicted time delays exhibit coherent and non-negligible shifts relative to the image-modelling-only case. The corrected BIC-weighted posteriors are

$$\Delta t_{AB}^{\text{EPL}} = -4.715_{-0.684}^{+0.623} \text{ days}, \quad \Delta t_{AB}^{\text{BPL}} = -5.722_{-0.844}^{+0.752} \text{ days}, \quad (43)$$

$$\Delta t_{AC}^{\text{EPL}} = -9.541_{-1.356}^{+1.250} \text{ days}, \quad \Delta t_{AC}^{\text{BPL}} = -11.643_{-1.718}^{+1.537} \text{ days}, \quad (44)$$

$$\Delta t_{AD}^{\text{EPL}} = -23.234_{-3.261}^{+3.025} \text{ days}, \quad \Delta t_{AD}^{\text{BPL}} = -28.815_{-4.306}^{+3.809} \text{ days}. \quad (45)$$

It can be seen that the differences in the relative time delays become even more pronounced after incorporating the kinematics and LOS corrections, reaching up to about 21–24%. To make explicit the effect of jointly sampling the internal mass profile and the LOS convergence, we compute the posterior distribution of the mass-sheet factor  $(1 - \kappa_{\text{ext}})\lambda_{\text{int}}$  (Fig. 10). The two families differ substantially: the EPL

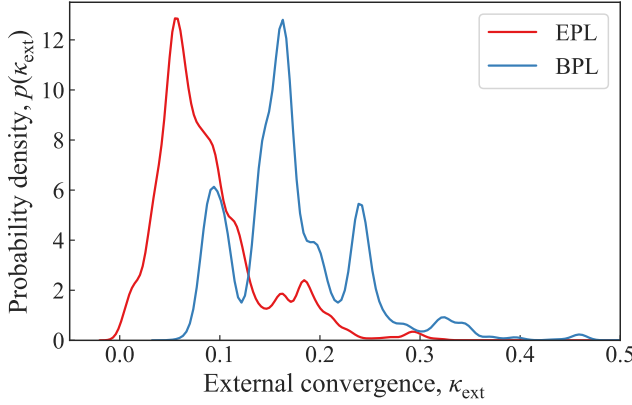


**Figure 9.** External-convergence distributions constructed following the Buckley–Geer et al. (2020) methodology, with additional weighting based on the predicted external shears for the EPL (red) and BPL (blue) model families. For each family, we consider multiple lens-model setups, compute the BIC weight of each setup, and map the sampled external-shear posterior  $\gamma_{\text{ext}}$  of that setup into a corresponding  $\kappa_{\text{ext}}$  distribution using the Buckley–Geer calibration. The illustrated curves are BIC-weighted combinations of these multiple  $\kappa_{\text{ext}}$  distributions.

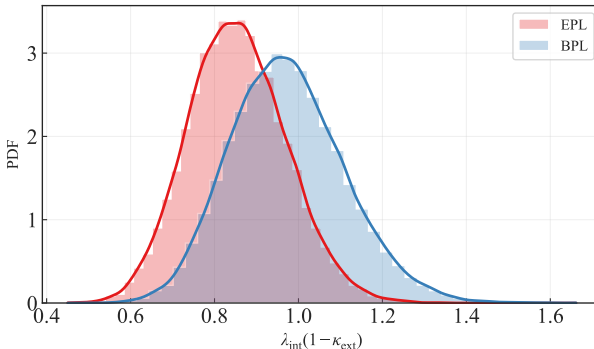


**Figure 10.** Posterior of the mass-sheet factor  $(1 - \kappa_{\text{ext}})\lambda_{\text{int}}$  for the EPL and BPL model families. The EPL family predicts a median of 0.851, whereas the BPL family favours 0.966.

model yields a median of  $0.851 \pm 0.117$ , while the BPL model gives  $0.966 \pm 0.138$ . These offsets demonstrate that the kinematics–LOS combination reshapes the effective time-delay scaling in a model-dependent manner, amplifying the differences already present in the image-modelling-only predictions.

Taken together, the corrected  $\Delta t$  posteriors and the inferred mass-sheet factors show that the two model families retain distinct cosmographic implications for the inferred time-delay distance and  $H_0$  even after incorporating all available non-imaging information. Although the stellar kinematics and the  $D_s/D_{\text{ds}}$  prior provide independent observational constraints, both  $\lambda_{\text{int}}$  and  $\kappa_{\text{ext}}$  are inferred quantities that remain conditional on the adopted lens mass model. Consequently, the resulting mass-sheet factor  $(1 - \kappa_{\text{ext}})\lambda_{\text{int}}$  should be interpreted as the outcome of a joint, model-dependent inference, rather than as an independent criterion for assessing the physical preference of a given mass-profile family.

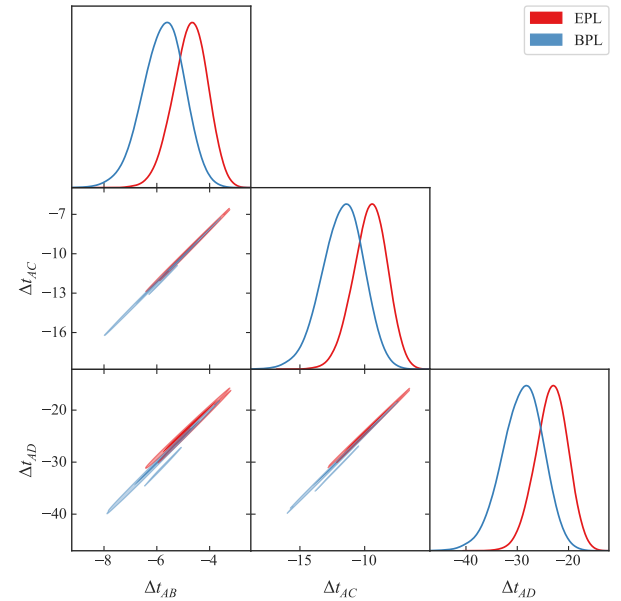


**Figure 11.** Corner plot of the model-predicted relative time delays (days) for the three pairs (AB, AC, AD). Chains are truncated to their last  $N = 1000$  samples, run weights are distributed uniformly over retained samples, and BPL (red) and EPL (blue) families are overplotted with filled contours. (Assuming flat  $\Lambda$ CDM cosmology with  $H_0 = 70 \text{ km s}^{-1} \text{ Mpc}^{-1}$  and  $\Omega_m = 0.3$ )

**Table 3.** Comparison of BIC-weighted model parameters. Quoted values are medians and 68% credible intervals. Note that here,  $\theta_E$  refers to the spherical-equivalent Einstein radius (i.e., effective Einstein radius).

Parameter	EPL model	BPL model
$\gamma$ (slope)	$2.30 \pm 0.02$	$2.43 \pm 0.02$
$\alpha$ (outer slope)	—	$2.799 \pm 0.066$
$\alpha_c$ (inner slope)	—	$1.26 \pm 0.06$
$r_c$ (arcsec)	—	$0.40 \pm 0.08$
$\theta_E$ (arcsec)	$1.380 \pm 0.001$	$1.364 \pm 0.004$
$q_m$ (axis ratio)	$0.600 \pm 0.005$	$0.650 \pm 0.02$
$\gamma_{\text{ext}}$	$0.077 \pm 0.004$	$0.119 \pm 0.004$

#### 6.4 Combine time-delay measurements

We now construct the time-delay distance posterior by combining the BIC-weighted posterior samples of the lens-model parameters and external convergence with the observed time delays (Wong et al. 2024). In that work, the time delays and their full covariance were inferred with the PyCS3 (Millon et al. 2020) curve-shifting analysis, where repeated optimizations with randomized initial shifts and mock light-curve realizations (including microlensing-like variability) yield a joint posterior from which the covariance is estimated; we therefore adopt the covariance matrix for delays relative to image A, which contains the full time-delay information. The time delays between images AB, AC, and AD are  $-12.4$ ,  $-5.3$ , and  $-33.3$  days, and the covariance matrix  $\mathbf{C}$  is shown in Table 4.

For each lens model sampling points we have the predicted (and MST-corrected) time delays  $\Delta t_{\text{fid}}$  under a fixed fiducial cosmology. In a general cosmology, the theoretical delays scale linearly with the

**Table 4.** Covariance matrix  $\mathbf{C}$  for the time delays between quasar images A, B, C, and D (units: days<sup>2</sup>).

Covariance (days <sup>2</sup> )	AB	AC	AD
AB	14.2	6.1	7.5
AC	6.1	14.8	7.1
AD	7.5	7.1	39.9

time-delay distance,

$$\Delta t_{\text{th}}(D_{\Delta t}) = R \Delta t_{\text{fid}}, \quad R \equiv \frac{D_{\Delta t}}{D_{\Delta t}^{\text{fid}}}, \quad (46)$$

where  $D_{\Delta t}^{\text{fid}}$  is computed under the fiducial flat  $\Lambda$ CDM cosmology as

$$D_{\Delta t}^{\text{fid}} = \left[ (1 + z_d) \frac{D_d D_s}{D_{ds}} \right]_{\text{fid}}. \quad (47)$$

The likelihood of the observed time-delay vector  $\mathbf{d} \equiv \Delta t_{\text{obs}}$ , with covariance matrix  $\mathbf{C}$ , can be written as

$$\mathcal{L}_{\Delta t_{\text{obs}}}(\mathcal{D}_{\Delta t_{\text{obs}}} \mid \xi_{\text{model}}, \kappa_{\text{ext}}, D_{\Delta t}) \propto \exp\left[-\frac{1}{2} \chi^2(R)\right], \quad (48)$$

where  $R \equiv D_{\Delta t}/D_{\Delta t}^{\text{fid}}$  and

$$\chi^2(R) = (\mathbf{d} - R \Delta t_{\text{fid}})^T \mathbf{C}^{-1} (\mathbf{d} - R \Delta t_{\text{fid}}). \quad (49)$$

The full posterior of the time-delay distance is obtained by marginalising over the lens-model and LOS degrees of freedom:

$$p(D_{\Delta t} \mid \mathcal{D}) \propto \int \mathcal{L}_{\Delta t_{\text{obs}}}(\mathcal{D}_{\Delta t_{\text{obs}}} \mid \xi_{\text{model}}, \kappa_{\text{ext}}, D_{\Delta t}) \times p(\xi_{\text{model}}, \kappa_{\text{ext}} \mid \mathcal{D}_{\text{img,kin,LOS}}) d\xi_{\text{model}} d\kappa_{\text{ext}}, \quad (50)$$

where the distribution  $p(\xi_{\text{model}}, \kappa_{\text{ext}} \mid \mathcal{D}_{\text{img,kin,LOS}})$  is represented numerically by the BIC-weighted posterior samples from the imaging, kinematic, and LOS inference. In practice, this marginalisation is performed by importance sampling over these model samples and summing their contributions:

$$p(D_{\Delta t} \mid \mathcal{D}) \propto \sum_n w_n \mathcal{L}_{\Delta t_{\text{obs}}}(\mathcal{D}_{\Delta t_{\text{obs}}} \mid \xi_{\text{model},n}, \kappa_{\text{ext},n}, D_{\Delta t}), \quad (51)$$

with  $w_n$  denoting the BIC weights. Since in our analysis the cosmology is restricted to flat  $\Lambda$ CDM with fixed  $\Omega_m$ , the mapping between  $D_{\Delta t}$  and  $H_0$  is strictly monotonic,  $D_{\Delta t} \propto H_0^{-1}$ . The posterior of  $H_0$  therefore follows directly from a change of variables applied to the sampled  $D_{\Delta t}$  distribution. The resulting posteriors show a statistically significant model dependence. For the EPL family, we obtain  $D_{\Delta t} = 1.603^{+0.443}_{-0.387}$  Gpc, corresponding to  $H_0 = 61.1^{+19.2}_{-13.2} \text{ km s}^{-1} \text{ Mpc}^{-1}$ . In contrast, the BPL family yields  $D_{\Delta t} = 1.297^{+0.362}_{-0.314}$  Gpc, implying  $H_0 = 75.2^{+23.0}_{-16.3} \text{ km s}^{-1} \text{ Mpc}^{-1}$ . These posterior distributions are illustrated in Figs. 12 and 13. Consistent with the discussion in Sect. 6.3, these differences reflect the model-dependent outcome of the joint lensing, kinematic, and LOS inference, rather than an independent validation of a specific mass-profile family. We emphasize that the observed shift in the inferred  $H_0$  between the EPL and BPL model families should be interpreted primarily as a manifestation of increased model flexibility under the mass-sheet degeneracy, rather than as direct evidence for a physical core in the inner mass distribution of the lens galaxy. While the BPL parameterization allows for a shallower inner slope, the current

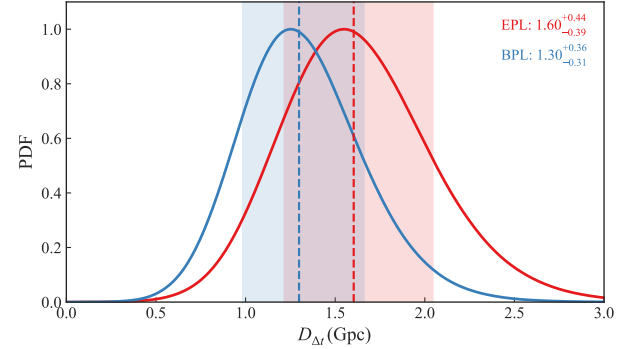


**Figure 12.** BIC-weighted one-dimensional posteriors of the time-delay distance  $D_{\Delta t}$  for the EPL (red) and BPL (blue) model families. For each lens-model sample, the Fermat-potential differences—after incorporating the  $(1 - \kappa_{\text{ext}})\lambda_{\text{int}}$  correction—are combined with the observed inter-image delays and their full covariance, yielding a Gaussian posterior in the scaling factor  $R = D_{\Delta t}/D_{\Delta t}^{\text{fid}}$ . The final  $D_{\Delta t}$  distributions are obtained by drawing from the corresponding Gaussian mixture over all model samples, weighted by their BIC likelihoods. Medians and 68% credible intervals are annotated.

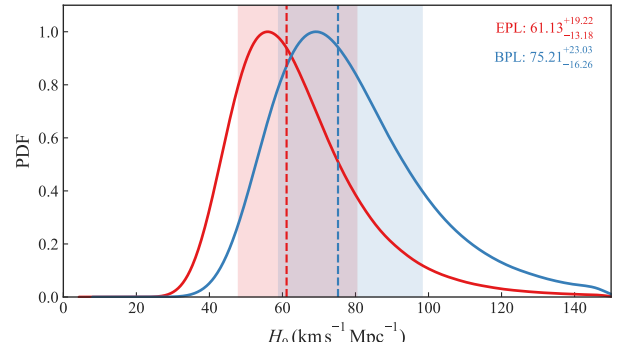


**Figure 13.** Posteriors of  $H_0$  obtained by mapping the  $D_{\Delta t}$  samples in Fig. 12 to the Hubble constant under a flat  $\Lambda$ CDM cosmology with fixed  $\Omega_m = 0.3$ . Because  $D_{\Delta t} \propto H_0^{-1}$  at fixed  $(z_{\ell}, z_s) = (0.228, 0.777)$ , the  $H_0$  posterior follows directly from a change of variables applied to the sampled  $D_{\Delta t}$  distribution. The inferred differences between the EPL (red) and BPL (blue) families reflect the model-dependent impact of their respective  $(1 - \kappa_{\text{ext}})\lambda_{\text{int}}$  corrections. Medians and 68% credible intervals are annotated.

imaging and kinematic data do not uniquely constrain the mass profile at radii well below the effective Einstein radius. Consequently, the difference in  $H_0$  reflects how different model families explore the allowed degeneracy space when combined with stellar kinematics and external convergence constraints, rather than a definitive detection of core-like structure.

## 7 RESULT EXPLANATION

As discussed in Sect. 6.2, although the time delay is formally determined by differences in the Fermat potential, the dominant contribution to the time-delay difference between the EPL and BPL model families arises from the geometric term. In this section, we provide supplementary diagnostics of the lensing potential, deflection angles,

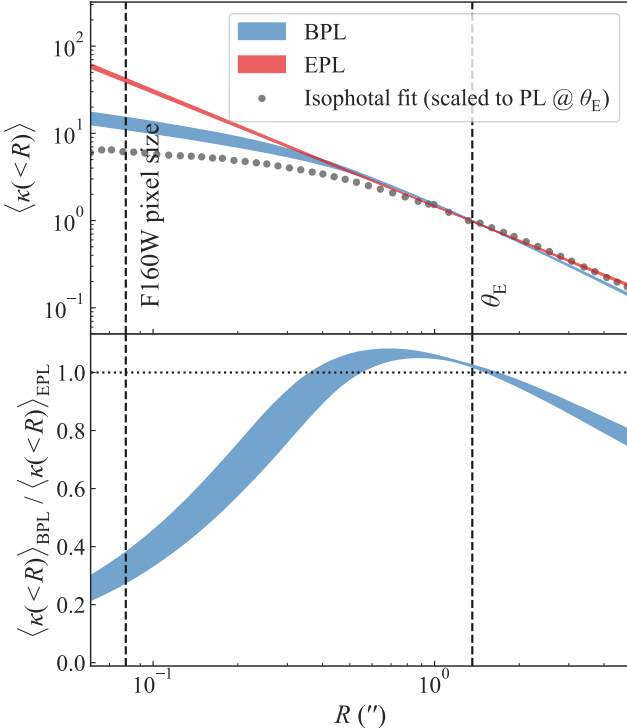


**Figure 14.** Comparison of the azimuthally averaged convergence profile,  $\langle \kappa \rangle$ , between the BPL and EPL models. The **top panel** shows the radial dependence of the mean projected mass within radius  $R$ . The red band represents the BIC weighted posterior, while the blue shaded region shows the BPL posterior. The grey dots indicate the best-fitting isophotal light profile scaled to match the EPL normalization at the Einstein radius  $\theta_E$ . Vertical dashed lines denote the HST/F160W pixel scale (left) and the median Einstein radius (right). At small radii, the two models exhibit different inner slopes, while they converge near and beyond  $\theta_E$ . The **bottom panel** displays the ratio  $\langle \kappa(< R) \rangle_{\text{BPL}} / \langle \kappa(< R) \rangle_{\text{EPL}}$ , highlighting the relative deviation between the two models as a function of radius. The shaded region encloses the  $1\sigma$  confidence interval of the BPL posterior.

and stellar-kinematic predictions to illustrate this point and to provide physical intuition for the model-dependent trends discussed in the main text.

Fig. 14 compares the azimuthally averaged projected mass distributions for the two model families. By construction, both models are constrained to reproduce the observed image configuration and the projected mass distribution near the Einstein radius. At smaller radii, however, the EPL and BPL models exhibit different inner radial behaviours, reflecting their distinct parameterizations of the mass profile. These differences lead to modest variations in the enclosed mass in the central regions, while the profiles converge near and beyond the Einstein radius.

To examine how these structural differences manifest at the image positions, we compute the lens potential and deflection angle profiles for both models using the best-fit parameters from the minimum-BIC realizations. The inferred image positions differ by less than  $0''.003$  between the two models, confirming that the image geometry is nearly identical. Consistent with this, the differences in the lens potential  $\Delta\psi$  evaluated at the image positions are very similar for the EPL and BPL models, with BPL-to-EPL ratios close to unity (see Fig. 15).

In contrast, the deflection angle profiles exhibit more pronounced differences between the two model families at the image radii, as

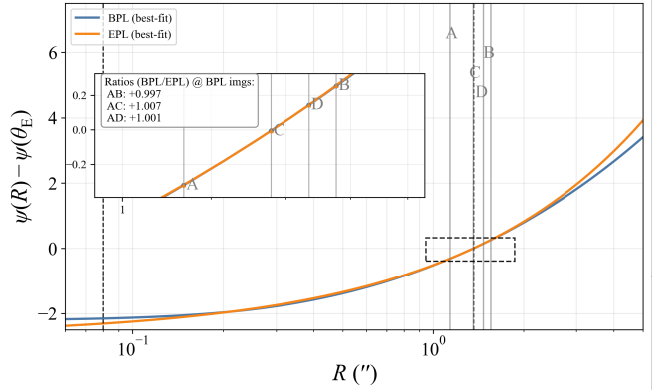


**Figure 15.** Lens potential comparison for image pairs AB, AC, and AD under the BPL and EPL models, using the best-fit parameters from the minimum-BIC realizations. The solid lines show the azimuthally averaged lens potential  $\psi(R)$ , plotted relative to  $\psi(\theta_E)$ , where  $\theta_E$  is the median Einstein radius from the BPL BIC-weighted results. Vertical dashed lines mark the HST/F160W pixel scale (left) and  $\theta_E$  (right), while the solid vertical lines indicate the image radii  $R_i$  ( $i = A, B, C, D$ ). The inset highlights the region around the image positions.

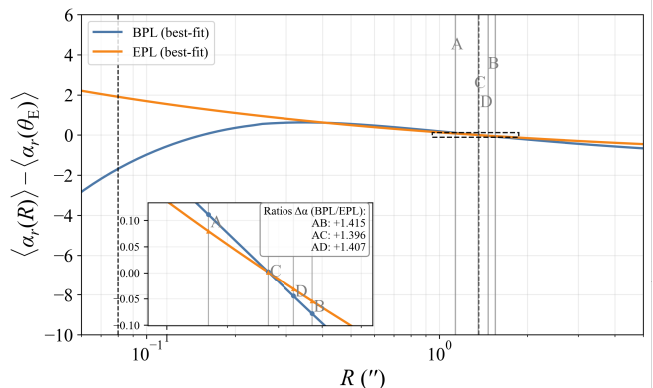


**Figure 16.** Deflection angle comparison for image pairs AB, AC, and AD under the BPL and EPL models, using the best-fit parameters from the minimum-BIC realizations. The solid lines show the azimuthally averaged deflection angles  $\alpha_r(R)$ , plotted relative to  $\alpha_r(\theta_E)$ . Vertical dashed lines mark the HST/F160W pixel scale (left) and  $\theta_E$  (right), while the solid vertical lines indicate the image radii. The inset highlights the region around the image positions.

illustrated in Fig. 16. These differences directly affect the geometric term of the Fermat potential and provide a natural explanation for why relatively small variations in the radial mass profile can translate into non-negligible differences in the model-predicted time delays, even when the lens potential itself remains similar at the image positions. These diagnostics therefore support the interpretation adopted in the main text that the time-delay differences are primarily driven by deflection-angle variations.

We additionally compare the posterior distributions of the stellar velocity dispersion predicted by the two model families. The velocity-dispersion posteriors shown in Fig. 17 are computed directly from the lens-model parameters using Eq. (27). To account for the full mass-sheet transformation, we then apply the  $(1 - \kappa_{\text{ext}})\lambda_{\text{int}}$  correction as prescribed by Eq. (29), and the resulting corrected pos-

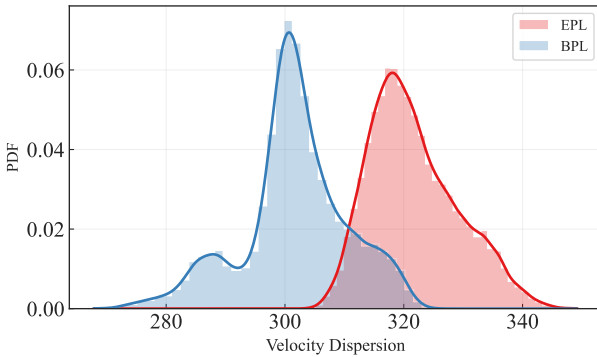


**Figure 17.** Posterior distributions of the stellar velocity dispersion without applying the  $(1 - \kappa_{\text{ext}})\lambda_{\text{int}}$  correction.

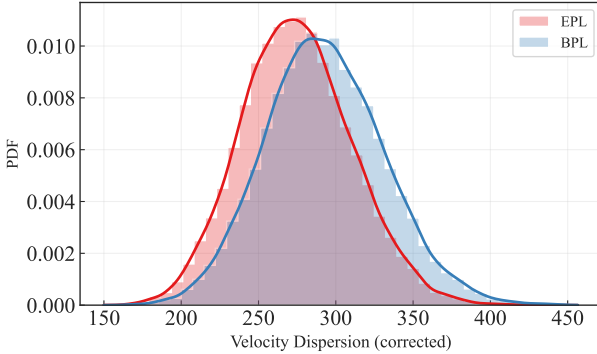


**Figure 18.** Posterior distributions of the stellar velocity dispersion after applying the  $(1 - \kappa_{\text{ext}})\lambda_{\text{int}}$  correction.

teriors are shown in Fig. 18. These figures show that, once the full mass-sheet correction is applied, both models can be brought into consistency with the observed kinematic constraints. Differences in the shapes of the posterior distributions reflect how the assumed mass profile interacts with the kinematic information and the line-of-sight convergence within the joint inference framework.

For further illustration, we also plot the circularized LOS velocity dispersion profiles,  $\sigma_{\text{los}}(R)$ , implied by the best model set (with minimal BIC value) for each family, shown in Fig. 19. Compared to the more sharply peaked central prediction of the EPL model, the BPL model yields a noticeably flatter inner profile within  $R \lesssim 0''25$  and even shows a mild downturn at the smallest radii. Interestingly, spatially resolved observations of nearby massive early-type galaxies do include cases with an approximately flat central velocity dispersion followed by a decline at larger radii (Veale et al. 2018). At  $R \gtrsim 0''35$ , however, the two profiles nearly overlap and are in excellent agreement. Nonetheless, the innermost  $\lesssim 0''2$  region is particularly susceptible to PSF and pixel size, and these profiles primarily highlight potential differences in the predicted kinematic behaviour under the model degeneracies.

The comparisons presented in this section are intended to illustrate the internal consistency of the modelling and to provide physical intuition for how mass-profile flexibility influences lensing and kinematic observables. They support the interpretation adopted in

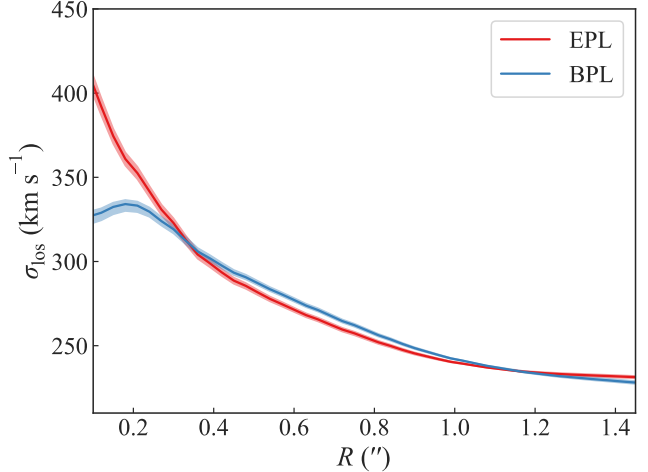


**Figure 19.** The circularized line-of-sight velocity-dispersion profile,  $\sigma_{\text{los}}(R)$ , is shown as a function of projected radius  $R$ , where the red and blue curves correspond to the EPL and BPL models, respectively. The solid lines and shaded bands denote the posterior median and the  $1\sigma$  credible range. We use the posterior samples from the BIC-selected best model set and predict the quantity measured in the IFU annular bins, assuming isotropic stellar orbits and a negligible PSF. The BPL model exhibits a noticeably flatter central velocity dispersion profile and shows a slight decrease near the innermost radius.

the main text that the differences between the EPL and BPL results arise from model-dependent assumptions about the mass distribution, rather than from artefacts of light-profile modelling, PSF treatment, or numerical implementation.

## 8 CONCLUSIONS

In this work, we have developed and implemented a Broken Power Law (BPL) mass profile within the LENSTRONOMY framework, together with a numerical solver for the lensing potential and time delays. We validated the numerical implementation in the limit of EPL where we have the analytical expression. The results demonstrate excellent agreement, confirming the high accuracy of the numerical method. We then applied the BPL model to a realistic lensed quasar system, namely WGD 2038–4008, incorporating multi-band imaging data, stellar kinematics, and LOS environmental information. For comparison, we also apply the EPL mass model to the same system, reproducing the result of Shajib et al. (2022).

Both the EPL and BPL models are capable of reproducing the observed lensed morphology and image configurations with comparable quality, indicating that the current imaging data alone are not able to uniquely determine the inner mass profile of the lens galaxy. In the absence of a clearly detected central image, lensing image data could merely constrain the projected mass distribution near the Einstein radius, while providing weak sensitivity to the mass profile at radii well inside this scale. When stellar kinematics and LOS external convergence are incorporated to constrain the mass-sheet degeneracy, the two model families yield time-delay distances that differ at the  $\sim 20\text{--}25\%$  level, with  $D_{\Delta t}^{\text{EPL}} = 1.603_{-0.387}^{+0.443}$  Gpc and  $D_{\Delta t}^{\text{BPL}} = 1.297_{-0.314}^{+0.362}$  Gpc. These differences propagate into the inferred Hubble constant, leading to  $H_0^{\text{EPL}} = 61.1_{-13.2}^{+19.2}$   $\text{km s}^{-1} \text{Mpc}^{-1}$  and  $H_0^{\text{BPL}} = 75.3_{-16.3}^{+23.0}$   $\text{km s}^{-1} \text{Mpc}^{-1}$  under a flat  $\Lambda\text{CDM}$  cosmology with fixed  $\Omega_{\text{m}} = 0.3$ .

Importantly, the dominant contribution to this shift in  $H_0$  does not arise from a direct measurement of the innermost mass distribution, but rather from differences in the effective mass profile in the vicinity of the Einstein radius once the internal mass-sheet factor is constrained by stellar kinematics. The additional radial flexibility of the BPL parameterization allows for a redistribution of mass at small radii that remains consistent with the imaging constraints near the Einstein scale, and this redistribution propagates through the mass-sheet degeneracy into the inferred time-delay distance. For a single lens system, the resulting uncertainties remain substantial; nevertheless, this comparison illustrates that assumptions about the lens mass profile alone can induce systematic variations in inferred cosmological parameters at a level that is non-negligible in the context of current precision goals in time-delay cosmography.

The combined impact of internal mass-profile flexibility and LOS convergence can be summarized through the effective mass-sheet factor  $\Lambda_{\text{tot}} = (1 - \kappa_{\text{ext}})\lambda_{\text{int}}$ . The inferred  $\Lambda_{\text{tot}}$  distributions differ between the EPL and BPL families, reflecting how internal profile assumptions and environmental convergence trade off along the mass-sheet degeneracy. As emphasized throughout this work, both  $\lambda_{\text{int}}$  and  $\kappa_{\text{ext}}$  are inferred quantities that remain conditional on the adopted mass model. The resulting  $\Lambda_{\text{tot}}$  should therefore be interpreted as the outcome of a joint, model-dependent inference rather than as an independent criterion for selecting a preferred physical description of the lens galaxy.

Comparisons presented in the Sect. 7, including diagnostics of the Fermat potential, deflection angles, stellar velocity dispersion, and PSF residuals (Appendix B), further support the internal consistency of the modeling and provide physical intuition for the origin of these model-dependent trends, without independently discriminating between the two mass-profile families.

Our results are broadly consistent with previous strong-lensing analyses of WGD 2038–4008 that employed different modeling frameworks and assumptions (e.g., Shajib et al. 2019, 2022), and they echo earlier findings that time-delay measurements of individual lens systems can exhibit non-negligible sensitivity to mass-profile systematics (e.g., Schneider & Sluse 2013; Chen et al. 2021; Blum et al. 2020). While such effects do not allow one to draw conclusions regarding the resolution of the Hubble tension, they underscore the importance of flexible mass modeling and explicit marginalization over profile uncertainties in precision time-delay cosmography.

Overall, this study highlights that internal mass-profile systematics constitute a significant source of uncertainty in time-delay cosmography for individual lenses. Flexible mass models, combined with a consistent treatment of stellar kinematics and LOS effects, are therefore essential for robust cosmological inference, particularly in future hierarchical analyses that combine multiple lens systems within a unified modeling framework.

## ACKNOWLEDGEMENTS

We thank Tian Li for valuable discussions and for sharing insights on numerical strategies for computing the Fermat potential integral. We are grateful to Simon Birrer and Anowar J. Shajib for making the LENSTRONOMY-based modelling tools publicly available. In particular, we thank Anowar J. Shajib for helpful correspondence on the modelling of WGD 2038–4008. We also thank Alessandro Sonnenfeld for insightful comments. This work is supported in part by the National Natural Science Foundation of China Grants No. 12333001, No. 12541301 and No. 12541302 and by the China Manned Spaced (CMS) program with grant Nos.

CMS-CSST-2025-A02, CMS-CSST-2025-A03, CMS-CSST-2025-A04 and CMS-CSST-2025-A20.

## DATA AVAILABILITY

The lens-modelling pipeline used in this work is built upon the publicly available software LENSTRONOMY (Birrer & Amara 2018). Readers can download the code at <https://github.com/WhosRick/lenstronomy.git>. We maintain a public fork of the main LENSTRONOMY repository in which we implemented the Broken Power-Law (BPL) mass profile. Although the corresponding pull request has not yet been merged into the upstream code base, the implementation is openly accessible and can be installed directly from our fork.

The HST imaging data for the quadruply imaged quasar WGD 2038–4008 analysed in this paper are available from the Mikulski Archive for Space Telescopes (MAST) under programme HST-GO-15320. We follow the HST lens-processing workflow described by Tan et al. (2024) for data retrieval and preprocessing. The derived data products from our analysis (e.g. model posteriors, reconstructed source images, and related summary products) will be made available upon reasonable request to the corresponding author.

Our overall analysis closely follows the publicly released TD-COSMO modelling framework for WGD 2038–4008 (Shajib et al. 2022) and is executed primarily in JUPYTER notebooks (Kluyver et al. 2016). For image download and preprocessing, we used ASTROQUERY (Ginsburg et al. 2019) and DRIZZLEPAC (Fruchter & et al. 2010), together with ASTROOBJECTANALYSER<sup>4</sup>. The lens modelling, posterior analysis, and figure production rely on LENSTRONOMY (Birrer et al. 2015; Birrer & Amara 2018; Birrer et al. 2021) and the fast elliptical deflection-angle implementation FASTELL4PY<sup>5</sup>, which wraps the original Fortran FASTELL code (Barkana 1999). Parameter inference and posterior visualisation make use of EMCEE (Foreman-Mackey et al. 2013), DYNESTY (Skilling 2004; Speagle 2020), and GETDIST<sup>6</sup>. Additional analysis utilities include PHOTUTILS (Bradley et al. 2020), SEABORN (Waskom et al. 2014), and COLOSSUS (Diemer 2018).

Throughout the workflow we used standard scientific Python packages, including NUMPY (Oliphant 2015), SCIPY (Jones et al. 2001), ASTRONY (Astropy Collaboration 2013, 2018), SExtractor (Bertin & Arnouts 1996), PANDAS (McKinney 2010), and MATPLOTLIB (Hunter 2007). We further used COLORIPY<sup>7</sup> and PAPERFIG<sup>8</sup> for colour maps and publication-style figure utilities.

## REFERENCES

Abbott T. M. C., Abdalla F. B., Annis J., et al. (DES Collaboration) 2018, *MNRAS*, 480, 3879  
 Addison G. E., Watts D. J., Bennett C. L., et al. 2018, *ApJ*, 853, 119  
 Agnello A., Schechter P. L., Morgan N. D., et al. 2018, *MNRAS*, 475, 2086  
 Astropy Collaboration 2013, *A&A*, 558, A33  
 Astropy Collaboration 2018, *AJ*, 156, 123  
 Barkana R., 1998, *ApJ*, 502, 531  
 Barkana R., 1999, ASCL, ascl:9910.003  
 Bertin E., Arnouts S., 1996, *A&AS*, 117, 393  
 Birrer S., Amara A., 2018, *Physics of the Dark Universe*, 22, 189

<sup>4</sup> <https://github.com/sibirrer/AstroObjectAnalyser>

<sup>5</sup> <https://github.com/sibirrer/fastell4py>

<sup>6</sup> <https://github.com/cmbant/getdist>

<sup>7</sup> <https://github.com/ajshajib/coloripy/tree/master>

<sup>8</sup> <https://github.com/ajshajib/paperfig>

Birrer S., Amara A., Refregier A., 2015, *ApJ*, **813**, 102

Birrer S., Amara A., Refregier A., 2016, *J. Cosmology Astropart. Phys.*, **2016**, 020

Birrer S., et al., 2020, *A&A*, **643**, A165

Birrer S., et al., 2021, *JOSS*, **6**, 3283

Blum K., Castorina E., Simonović M., 2020, *ApJ*, **892**, L27

Bradley L., et al., 2020, astropy/photutils: 1.0.0, Zenodo, doi:10.5281/zenodo.4044744, <https://doi.org/10.5281/zenodo.4044744>

Buckley-Geer E. J., Lin H., Rusu C. E., et al. 2020, *MNRAS*, **498**, 3241

Cappellari M., 2002, *MNRAS*, **333**, 400

Chen G. C.-F., et al. 2016, *MNRAS*, **462**, 3457

Chen G. C.-F., Fassnacht C. D., Suyu S. H., Yıldırım A., Komatsu E., Luis Bernal J., 2021, *A&A*, **652**, A7

Ciotti L., Bertin G., 1999, *A&A*, **352**, 447

Collaboration P., Aghanim N., Akrami Y., et al., 2020, *Astronomy & Astrophysics*, **641**, A6

Diemer B., 2018, *ApJS*, **239**, 35

Du W., Zhao G.-B., Fan Z., Shu Y., Li R., Mao S., 2020, *ApJ*, **892**, 62

Du W., Fu L., Shu Y., Li R., Fan Z., Shu C., 2023, *ApJ*, **953**, 189

Falco E. E., Gorenstein M. V., Shapiro I. I., 1985, *ApJ*, **289**, L1

Foreman-Mackey D., Hogg D. W., Lang D., Goodman J., 2013, *PASP*, **125**, 306

Freedman W. L., 2021, *ApJ*, **919**, 16

Fruchter A. S., et al. 2010, in 2010 Space Telescope Science Institute Calibration Workshop, pp 382–387

Gilman D., Bovy J., Treu T., Nierenberg A., Birrer S., Benson A., Sameie O., 2021a, *MNRAS*, **507**, 2432

Gilman D., Bovy J., Treu T., Nierenberg A., Birrer S., Benson A., Sameie O., 2021b, *MNRAS*, **507**, 2432

Gilman D., Zhong Y.-M., Bovy J., 2023, *Phys. Rev. D*, **107**, 103008

Ginsburg A., et al., 2019, *AJ*, **157**, 98

Hunter J. D., 2007, *Computing in Science and Engineering*, **9**, 90

Jee I., Komatsu E., Suyu S. H., Huterer D., 2019, *Science*, **365**, 1134

Jones E., Oliphant T., Peterson P., Others 2001, SciPy: Open source scientific tools for Python. <http://www.scipy.org/>

Kaplinghat M., Tulin S., Yu H.-B., 2016, *Phys. Rev. Lett.*, **116**, 041302

Keeton C. R., 2001, *astro-ph/0102340*

Keeton C. R., 2003, *ApJ*, **582**, 17

Kluyver T., et al., 2016, in Loizides F., Schmidt B., eds, *Positioning and Power in Academic Publishing: Players, Agents and Agendas*. IOS Press BV, Amsterdam, Netherlands, pp 87 – 90 (arXiv:IOS Press), doi:10.3233/978-1-61499-649-1-87

Lima Neto G. B., Gerbal D., Márquez I., 1999, *MNRAS*, **309**, 481

MacArthur L. A., Courteau S., Holtzman J. A., 2003, *ApJ*, **582**, 689

Mamon G. A., Łokas E. L., 2005, *MNRAS*, **363**, 705

Márquez I., Lima Neto G. B., Capelato H., Durret F., Lanzoni B., Gerbal D., 2001, *A&A*, **379**, 767

McKinney W., 2010, *SciPy 2010*

Merritt D., 1985, *AJ*, **90**, 1027

Millon M., Tewes M., Bonvin V., Lengen B., Courbin F., 2020, *The Journal of Open Source Software*, **5**, 2654

Muller S., Jaswanth S., Horellou C., Martí-Vidal I., 2020, *A&A*, **641**, L2

Navarro J. F., Frenk C. S., White S. D. M., 1997, *ApJ*, **490**, 493

Oliphant T. E., 2015, *Guide to NumPy*, second edn. CreateSpace Independent Publishing Platform, USA

Osipkov L. P., 1979, *Soviet Astronomy Letters*, **5**, 42

Perera D., Williams L. L. R., Scarlata C., 2023, *MNRAS*, **522**, 1863

Pesce D. W., Reid M. J., Braatz J. A., et al. 2020, *ApJ*, **891**, L1

Quinn J., et al., 2016, *MNRAS*, **459**, 2394

Refregier A., 2003, *MNRAS*, **338**, 35

Refregier A., Bacon D., 2003, *MNRAS*, **338**, 48

Riess A. G., Yuan W., Macri L. M., Zinn J. C., Scolnic D., et al., 2022, *Astrophysical Journal Letters*, **934**, L7

Schneider P., Sluse D., 2013, *A&A*, **559**, A37

Schramm T., 1990, *A&A*, **231**, 19

Scolnic D. M., et al., 2018, *ApJ*, **859**, 101

Sérsic J. L., 1963, *Boletin de la Asociacion Argentina de Astronomia La Plata Argentina*, **6**, 41

Sérsic J. L., 1968, *Atlas de Galaxias Australes*

Shajib A. J., et al., 2019, *MNRAS*, **483**, 5649

Shajib A. J., et al., 2020, *Monthly Notices of the Royal Astronomical Society*, **494**, 6072

Shajib A. J., et al., 2022, *A&A*, **667**, A123

Skilling J., 2004, in Fischer R., Preuss R., Toussaint U. V., eds, *American Institute of Physics Conference Series Vol. 735, Bayesian Inference and Maximum Entropy Methods in Science and Engineering: 24th International Workshop on Bayesian Inference and Maximum Entropy Methods in Science and Engineering*. AIP, pp 395–405, doi:10.1063/1.1835238

Sonnenfeld A., Cautun M., 2021, *A&A*, **651**, A18

Speagle J. S., 2020, *MNRAS*, **493**, 3132

Suyu S. H., Marshall P. J., Auger M. W., et al. 2010, *ApJ*, **711**, 201

Tan C. Y., et al., 2024, *MNRAS*, **530**, 1474

Tdcosmo Collaboration et al., 2025, *A&A*, **704**, A63

Terzić B., Graham A. W., 2005, *MNRAS*, **362**, 197

Tessore N., Metcalf R. B., 2015, *A&A*, **580**, A79

Tran V., Shen X., Vogelsberger M., Gilman D., O’Neil S., Roche C., Zier O., Gao J., 2024, *arXiv e-prints*, p. arXiv:2411.11945

Treu T., Koopmans L. V. E., 2004, *ApJ*, **611**, 739

Treu T., Marshall P. J., 2016, *The Astronomy and Astrophysics Review*, **24**, 11

Tulin S., Yu H.-B., 2018, *Physics Reports*, **730**, 1

Veale M., Ma C.-P., Greene J. E., Thomas J., Blakeslee J. P., Walsh J. L., Ito J., 2018, *MNRAS*, **473**, 5446

Vegetti S., et al., 2024, *Space Sci. Rev.*, **220**, 58

Verde L., Treu T., Riess A. G., 2019, *Nature Astronomy*, **3**, 891

Waskom M., et al., 2014, seaborn: v0.5.0 (November 2014), doi:10.5281/zenodo.12710, <https://doi.org/10.5281/zenodo.12710>

Wong K. C., Suyu S. H., Matsushita S., 2015, *ApJ*, **811**, 115

Wong K. C., Suyu S. H., Chen G. C. F., et al. 2020, *MNRAS*, **498**, 1420

Wong K. C., et al., 2024, *A&A*, **689**, A168

## APPENDIX A: LENS AND SOURCE LIGHT PROFILES

In this study, we use a combination of parametric and non-parametric light profiles to model the lens galaxy and the source galaxy. The lens light is modeled using a combination of multiple elliptical Sérsic profiles, while the source light is modeled using a Sérsic profile for the bulge component and a shapelet expansion for the extended light distribution. The details of these profiles are as follows:

- **Sérsic profile:** For the lens light in each band, we model the light distribution using a series of elliptical Sérsic profiles. The Sérsic profile is given by (Sérsic 1963, 1968):

$$I_{\text{Sérsic}}(r) = I_0 \exp \left[ -b_n \left( \frac{r}{r_{\text{eff}}} \right)^{1/n} \right], \quad (\text{A1})$$

where  $I_0$  is the central intensity,  $r_{\text{eff}}$  is the effective radius,  $n$  is the Sérsic index, and  $b_n$  is a constant that ensures that the effective radius encloses half the total flux. For the lens light, we use a combination of three elliptical Sérsic profiles for different bands, which adequately capture the lens galaxy’s light distribution.

- **Shapelets profile:** Shapelets provide a convenient basis to represent the surface brightness distribution of an extended source as a truncated linear expansion in localized, orthonormal functions. The Shapelets profile is given by (Refregier 2003; Refregier & Bacon 2003):

$$I(x, y) = \sum_{n_1+n_2 \leq n_{\text{max}}} f_{n_1, n_2} \psi_{n_1, n_2}(x, y; \beta), \quad (\text{A2})$$

where  $(x, y)$  are coordinates,  $\beta$  sets the characteristic spatial scale of the basis functions,  $f_{n_1, n_2}$  are the shapelet coefficients, and the expansion is truncated at total order  $n_{\max}$ . The number of coefficients in this truncation is

$$N_{\text{shapelets}} = \frac{(n_{\max} + 1)(n_{\max} + 2)}{2}, \quad (\text{A3})$$

corresponding to all integer pairs  $(n_1, n_2)$  with  $n_1 \geq 0$ ,  $n_2 \geq 0$ , and  $n_1 + n_2 \leq n_{\max}$ . In the Cartesian formulation, the 1D normalized Hermite functions are defined as

$$\phi_n(x) \equiv (2^n \sqrt{\pi} n!)^{-1/2} H_n(x) \exp\left(-\frac{x^2}{2}\right), \quad (\text{A4})$$

where  $H_n(x)$  is the Hermite polynomial of order  $n$  and  $x$  is a dimensionless coordinate. The 2D shapelet basis function is then given by the separable product

$$\psi_{n_1, n_2}(x, y; \beta) \equiv \phi_{n_1}\left(\frac{x}{\beta}\right) \phi_{n_2}\left(\frac{y}{\beta}\right). \quad (\text{A5})$$

- **PL-Sérsic profile:** In addition to the Sérsic and shapelets profiles, we also experimented with a hybrid “PL–Sérsic” profile for the lens light, which combines a power-law mass profile with a Sérsic light profile. The formula for the 2D PL-Sérsic profile is (Terzić & Graham 2005):

$$I(r) = \begin{cases} j_c \left(\frac{r}{r_c}\right)^{-\alpha_c} & \text{if } r \leq r_c, \\ j_0 \left(\frac{r}{s}\right)^{-u} \exp\left[-\left(\frac{r}{s}\right)^\nu\right] & \text{if } r \geq r_c, \end{cases} \quad (\text{A6})$$

where

$$j_0 = j_c \left(\frac{r_c}{s}\right)^u \exp\left[\left(\frac{r_c}{s}\right)^\nu\right], \quad (\text{A7})$$

where  $r_c$  is the break radius,  $j_c$  is the luminosity density at  $r_c$ , and  $s = \frac{R_{\text{eff}}}{k^n}$ , where  $k$  is a function of the Sérsic index  $n$  (Ciotti & Bertin 1999; MacArthur et al. 2003).  $\nu = 1/n$  and  $u = 1 - 0.6097 \nu + 0.054635 \nu^2$ , following Lima Neto et al. (1999); Márquez et al. (2001). This profile is intended to combine the effects of the mass distribution’s power-law (in the inner regions) and the Sérsic profile (in the outer regions). However, this profile did not perform as well in initial tests, likely due to insufficient code maturity or prior settings. We plan to revisit and improve the PL-Sérsic profile in future work, focusing on enhancing the fitting process and exploring its potential advantages for complex galaxy structures.

## APPENDIX B: PSF COMPARISON ACROSS EPL AND BPL MODELS

To assess the effect of different lens models on the PSF and residuals, we compare the PSF-convolved lens models (EPL vs. BPL) across the three imaging bands. The first column of Fig. B1 shows the PSF for the EPL family, the second column shows the corresponding PSF for the BPL family, and the third column shows the residuals obtained by subtracting the BPL PSF from the EPL PSF. These residuals provide a direct comparison between the two models.

The differences between the two models are minimal, indicating that both reproduce the PSF structure with comparable accuracy across all bands. As seen in the residual maps, the BPL model provides only a marginally better match in the central regions, but the improvement is negligible within the noise level. Overall, the PSF reconstructions are virtually indistinguishable, and the FWHM of the PSF is identical between the two models at the corresponding pixel scale.

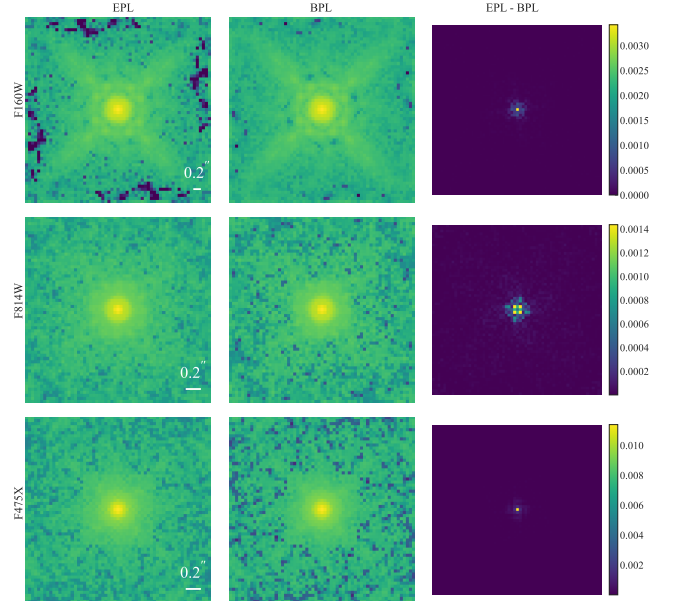


**Figure B1.** PSF comparison between the EPL (left column) and BPL (middle column) families across three bands. The third column shows the residuals obtained by subtracting the BPL PSF from the EPL PSF. The comparison highlights minor differences in the PSF, with the BPL model providing a slightly better fit to the observed data, particularly in the central regions.